PHILOSOPHICAL TRANSACTIONS OF THE ROYAL SOCIETY A
MATHEMATICAL, PHYSICAL & ENGINEERING SCIENCES

A Shear-Velocity Model of the Mantle [and Discussion]

Guy Masters, Stuart Johnson, Gabi Laske, Harold Bolton and J. H. Davies

Phil. Trans. R. Soc. Lond. A 1996 **354**, 1385-1411
doi: 10.1098/rsta.1996.0054

A shear-velocity model of the mantle

By Guy Masters, Stuart Johnson, Gabi Laske and Harold Bolton

IGPP, University of California at San Diego, La Jolla, CA 92093-0225, USA

We present a new model of shear velocity structure in the mantle which is designed to fit data-sets of absolute and differential body-wave travel times, surface-wave phase velocities over a broad range of frequencies, and structure coefficients of modes of free oscillation. The model is parametrized laterally by spherical harmonics (truncated at degree 16) and by 30 natural cubic B-splines in radius. Our best model features large-amplitude structure (up to ±6% anomalies in shear velocity) in the topmost 400 km of the mantle and in the lowermost 500 km (up to ±2.5%) with most of the power in the low harmonics ($\ell < 6$). The middle of the mantle is characterized by low-amplitude anomalies with a much whiter spectrum. Our models generally show no distinctive changes in structure (in either shape or amplitude) at the 660 km discontinuity supporting the idea that an endothermic phase transition is not a barrier to large-scale flow in the mantle.

1. Introduction

Many branches of geophysics would benefit from an accurate map of the three-dimensional structure of the mantle. Geochemists are interested in the correlation of isotopic anomalies with the seismic models, and geodynamicists are interested in using the models to constrain viscosity structure and characteristics of mantle flow. Seismology itself benefits by the improvement in realism in modelling wave propagation which then allows more detailed studies of the seismic source. While we are a long way from having an accurate global picture of mantle structure, it is now apparent that the spectrum of heterogeneity in the Earth is very red and it is reasonable to expect that accurate maps of the largest-scale structure are within our reach.

High-quality, long-period digital seismic data are now available for a timespan covering 15 years or more. Such data have been used in the past to construct models of mantle structure (Masters *et al.* 1982; Woodhouse & Dziewonski 1984; Nataf *et al.* 1986; Dziewonski & Woodhouse 1987; Tanimoto 1988, 1990; Su & Dziewonski 1991). Long-wavelength upper mantle structure has been quite well-determined since the early 1980s (Woodhouse & Dziewonski 1984) but it is only in the last two or three years that sufficiently large data-sets have been constructed so that the largest-scale features are becoming well-resolved throughout the mantle (Woodward *et al.* 1993; Masters *et al.* 1992; Su *et al.* 1994). Most of these studies have concentrated on the S-wave velocity structure (as we do here). P-wave structure has been mainly constrained using the short-period ISC travel time data-set (Dziewonski 1984; Inoue *et al.* 1990; Hager & Clayton 1989) though, recently, long-period P-wave data-sets

Phil. Trans. R. Soc. Lond. A (1996) **354**, 1385–1411

Printed in Great Britain

TEX Paper

have also been developed (Bolton & Masters 1991) and reliable joint inversions for P and S structure will shortly be available.

The long-period instruments of the Global Digital Seismic Network (GDSN) pass signals with a dominant period of about 20 s. Such waves have horizontal wavelengths of 100–200 km and their travel-time residuals exhibit much greater spatial coherence than the short period (about 1 Hz) data that make up the bulk of the large catalogues of travel times. We have experimented with using later-arriving phase data from the ISC data-set but generally find that such strong averaging is required to reveal any coherent large-scale signal that the effective geographical coverage of an ISC data-set is usually poorer than that of the equivalent GDSN data-set. Later arrivals in long-period data are usually much clearer than their short-period counterparts and the long-period stacks of Shearer (1990, 1991*a*, *b*) show many possible phases which have not yet been thoroughly analysed on a global scale. In short, the existing long-period body-wave data-set is an extremely rich one and provides many opportunities for significantly improving our knowledge of Earth structure. Inspection of all long-period recordings of earthquakes with body wave magnitude greater than 5.5 from 1976 to 1987 has resulted in a data-set of over 45 000 usable transverse component seismograms. Since 1987, there has been a significant expansion of the global network with the addition of the GEOSCOPE network and the various components of the IRIS program adding to the global coverage. Data from other arrays such as POSEIDON and MEDNET are also becoming available. The new stations, particularly in the Southern Hemisphere, promise much more uniformity in the sampling of the Earth than has been available to date.

This paper describes the current status of our research in developing data-sets of long-period body-wave differential and absolute travel times, surface-wave phase-velocity maps, and free-oscillation structure coefficients and using them to recover global-scale models of mantle structure. Given the rapid expansion of the global networks, it is unlikely that this will be the final word on the subject.

2. The data-sets

(*a*) *Absolute S times*

The main feature which distinguishes the current model from others in the literature is that the inclusion of a new data-set of long-period absolute S times with lower-mantle turning points significantly improves our resolution of lower-mantle structure. The measurement technique uses a cross-correlation of the data with a 'synthetic seismogram'. The synthetic is taken to be the impulse response of the instrument convolved with a t^* operator (Doornbos 1983). We concentrate on matching the first swing of the waveforms (figure 1) so that depth phases are unimportant for all but the shallowest earthquakes. Experiments with synthetic seismograms constructed using mode summation techniques indicate that the measurement algorithm is capable of a precision of 0.1 s. A subjective estimate of a typical measurement precision is about 0.5 s which is very competitive with other travel time catalogues. The polarity and amplitude of the arrival is recorded as well as the arrival time. Comparisons of the observed polarities with the predictions of the Harvard CMT solutions shows that the polarity is correctly predicted 88% of the time and suggests that half-cycle errors (*ca.* 12 s) are rare. About a third of the measurements with incorrectly predicted polarities are calculated to be near-nodal and small changes in

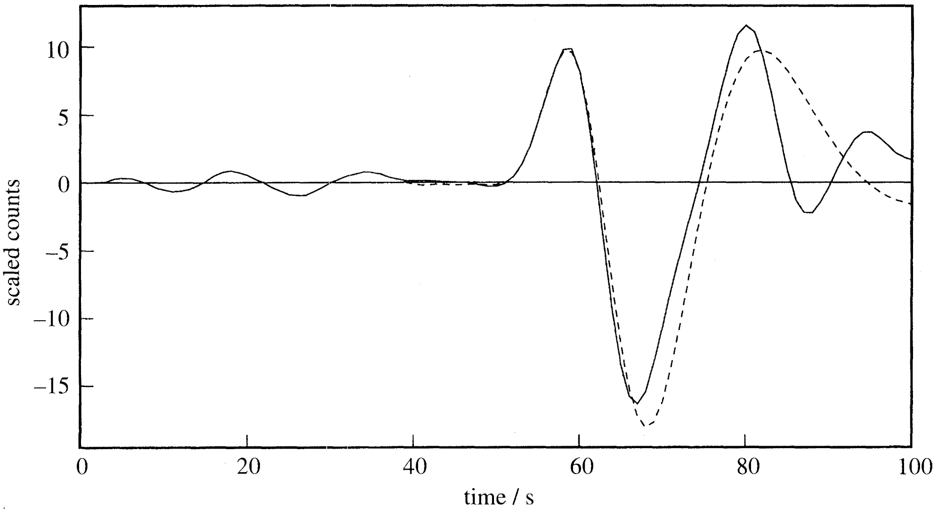

Figure 1. An example of the fit of a 'synthetic' S arrival to a transverse component seismogram recorded at the SRO station NWAO.

focal mechanism can accomodate these. Yet another third are associated with source mechanisms which incorrectly predict the majority of observed polarities (about 1% of the CMT catalogue) and the final third (about 4% of our total data-set) appear to be mispicked. We have collected a total of 23 000 S arrivals though we have analysed only lower-mantle turning rays in detail (about 18 000 S arrivals).

The data are first converted to ellipticity-corrected residuals relative to PREM using NEIC event locations. The raw residuals show strong distance and event-depth dependent trends which we interpret as being due to inadequacies in the assumed t^* operator and the use of NEIC locations with the PREM model. With this much data, it is simple to empirically determine these trends and remove them from the data-set. Histograms of residuals for the detrended S data are shown in figure 2 for a variety of turning-point depth ranges. Note the broadening of the S wave histograms for rays which turn in the lowermost mantle. If we plot the residuals of the deepest-turning rays at the turning point of the ray and lightly smooth the resulting map using a running mean in a spherical cap of radius 5°, we obtain the result shown in figure 3. The data show a remarkably coherent large-scale pattern which is in extremely good agreement with equivalent results for $ScS - S$ differential times shown in figure 4. (These $ScS - S$ differential times are an enlarged version of the data-set described by Woodward & Masters (1991*a*).) Figures 3 and 4 provide direct evidence for large-scale structure in shear velocity near the base of the mantle. The pattern in the data is one that implies a distribution of fast velocity anomalies near the core–mantle boundary under the rim of the Pacific. This pattern is similar to that seen in an early P-wave tomography model (L02.56 of Dziewonski 1984). It is also interesting to note that the amplitude of the travel-time anomalies in the S-wave data is larger than that in the $ScS - S$ data implying that shear velocity structure in the mid-mantle is mildly correlated with the structure at the base of the mantle.

(*b*) *Differential times*

An extensive study of $PP - P$ and $SS - S$ differential times was presented by Woodward & Masters (1991*b*) and these data-sets have continued to be expanded.

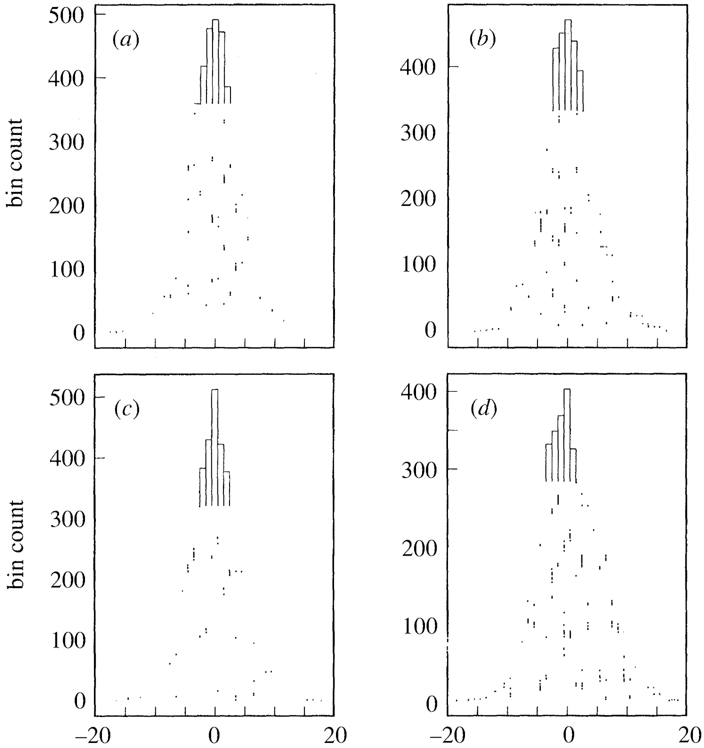

Figure 2. Histograms of the detrended S data in four ranges of turning depths in the lower mantle each about 550 km thick: (a) 650–1100 km, (b) 1100–1700 km, (c) 1700-2300 km, (d) 2300–2890 km. Note the increased variance of the deepest-turning S rays.

The data-sets have now achieved almost complete geographical coverage of bounce point locations and provide good control of the vertically averaged structure in the upper mantle. Comparisons of the $PP-P$ and $SS-S$ patterns are also interesting, showing that $SS-S$ residuals are typically three times the equivalent $PP-P$ value. We have tried a similar experiment with $PcP-P$ (Pulver & Masters 1990) for comparison with our extensive data-set of $ScS-S$, but the small number of reliable long-period $PcP-P$ measurements makes the comparison rather uncertain. A preliminary result shows that $PcP-P$ times are also typically three times smaller than the equivalent $ScS-S$ times (in agreement with an earlier regional study of Jordan & Lynn (1974)). While this ratio is not as extreme as some that have been proposed, if taken at face value it is barely in agreement with a thermal interpretation for the source of the velocity anomalies in the lower mantle (Karato 1993). It has therefore been suggested that lateral variations in composition are at least partly responsible for the velocity anomalies at the base of the mantle.

In the current inversion for S velocity, we use an expanded $SS-S$ data-set of 10 000 measurements and an $ScS-S$ data-set of about 5000 measurements. To give an idea of the coverage of the data-sets, figure 5a shows the smoothed $SS-S$ residual distribution with residuals plotted at the SS bounce point at the surface. This map shows a clear correlation with surface tectonics though we have previously shown that lower-mantle structure can contribute significantly to $SS-S$ travel times (Masters *et al.* 1993). In fact, if we use a shear-velocity model to calculate and remove the

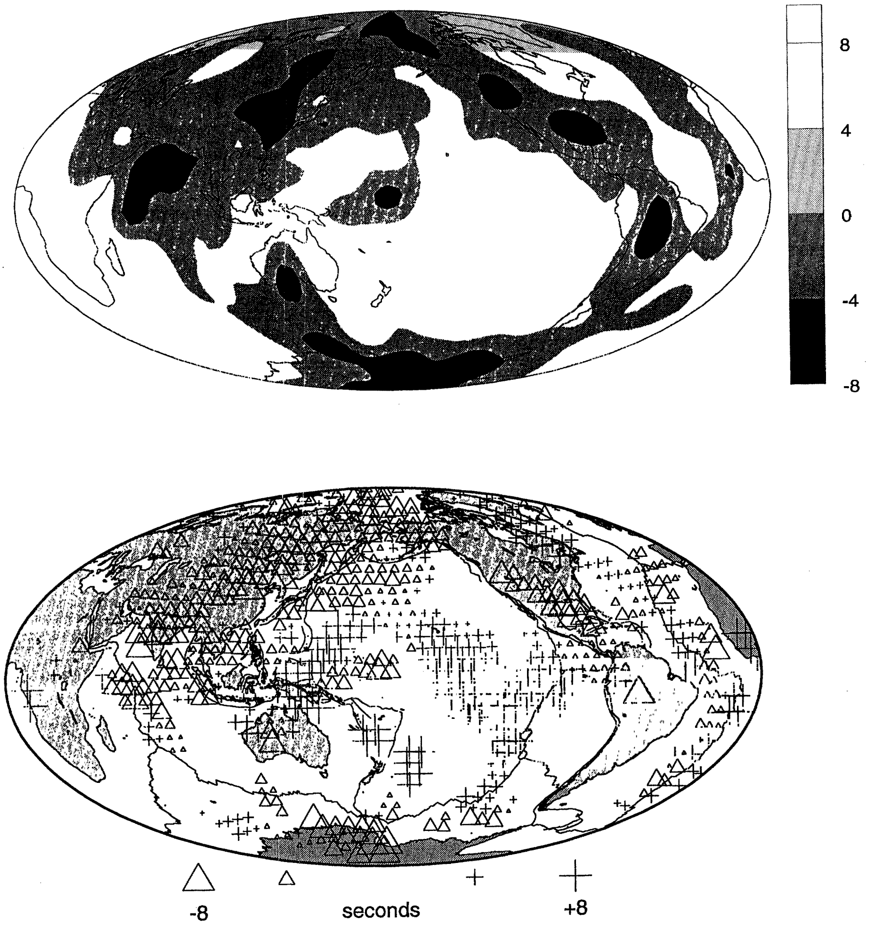

Figure 3. Lower panel: long-period S residuals plotted at the turning point of S for rays which bottom in the lowermost 300 km of the mantle. The raw data have been lightly smoothed by applying a running-mean smoothing filter which is a spherical cap of radius 5°. Note the ring of negative residuals (fast velocity) around the Pacific. The upper panel shows a map of the data constructed using spherical splines. The contour levels are in seconds.

effects of lower mantle structure, we arrive at the map shown in figure 5*b* (this map uses model SH8/U4L8 of Forte *et al.* (1993) but similar results are obtained with our models). This map now shows much clearer correlation with surface tectonics – in particular, the correlation with the age of the oceanic lithosphere is now quite dramatic (Masters *et al.* 1993) and suggests we should correct for this signal in the future.

(*c*) *Phase-velocity maps*

Global surface wave inversions have been carried out by numerous workers by either measuring surface wave dispersion (Montagner & Tanimoto 1991) or modelling long-period waveforms (Woodhouse & Dziewonski 1984; Tanimoto 1988). We prefer the use of dispersion data since errors are more easily assigned and an independent evaluation of a proper parametrization for upper mantle structure is possible. The transfer function technique we use for phase estimation involves measuring phase and

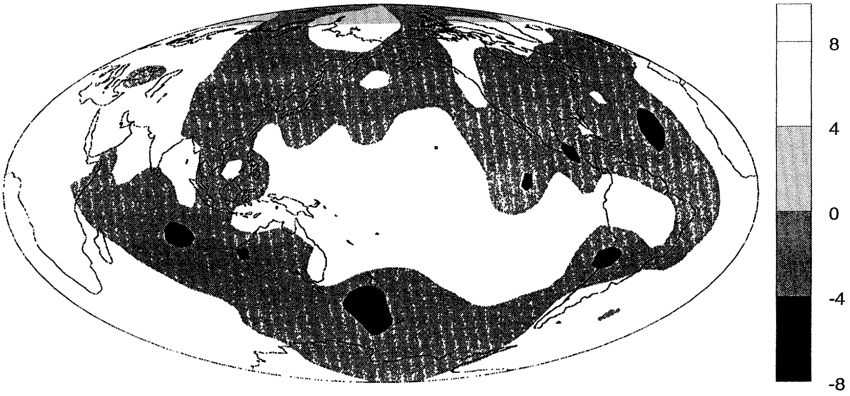

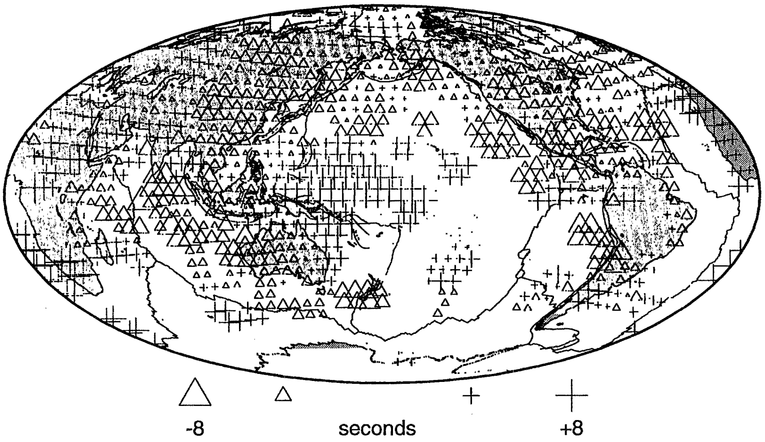

Figure 4. Long-period $ScS - S$ residuals plotted at the bounce point of ScS on the core–mantle boundary (see figure 3 for details). Again, note the ring of negative residuals (fast velocity) around the Pacific.

amplitude relative to a synthetic waveform which has been optimally aligned with the data. The technique is based on multi-taper spectral estimation (Thomson 1982) and is robust and allows an estimate of measurement errors (Laske 1993). To date, we have collected a total of about 10 000 phase measurements for the first two wave trains (R1, R2, G1, G2) and for great circle pairs (R3-R1, R4-R2, G3-G1, G4-G2) at each of various periods between 250 and 70 s (Laske & Masters 1996).

Inversions for surface-wave phase-velocity maps are dramatically improved by the addition of polarization data (i.e. the arrival angle of the incoming surface wave packet). Such data are sensitive to the lateral derivative of phase velocity and so aid in the recovery of short wavelength structure. Our polarization measurement technique closely follows Park *et al.* (1987) except in some minor respects (Laske 1993) and gives a reliable measure of the frequency-dependent arrival angle of the surface-wave packet. Ray tracing calculations show that Woodhouse & Wong's (1986) linear theory for the off-great circle arrival angle is sufficiently accurate for realistic long-wavelength phase velocity variations (up to $\ell = 16$) to explain the observed

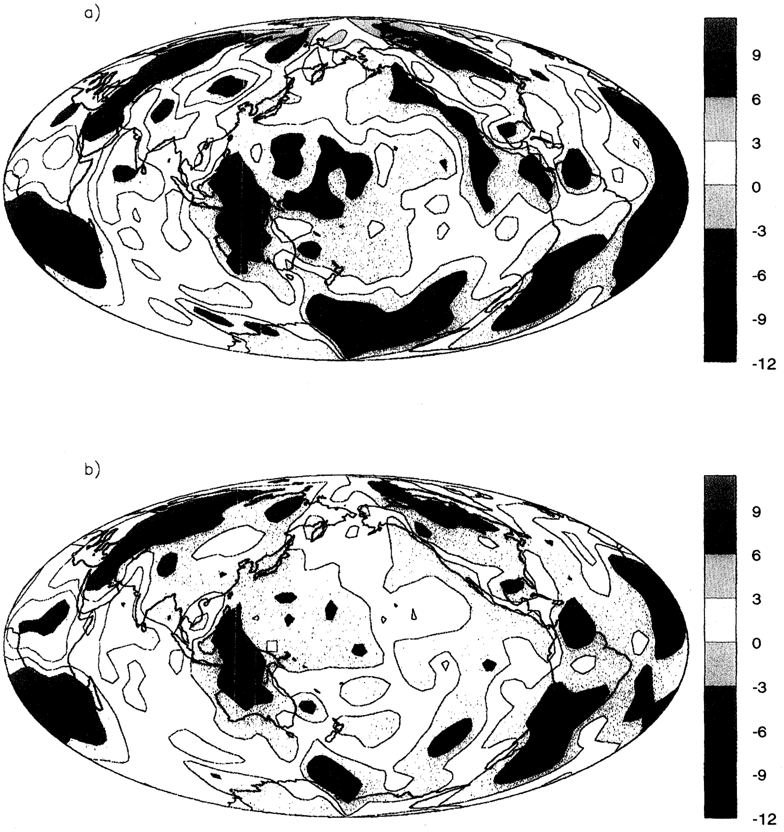

Figure 5. Smoothed $SS - S$ residuals relative to PREM, constructed by fitting spherical splines to $SS - S$ residuals placed at their surface bounce points. Contour levels are in seconds. (*a*) is corrected for ellipticity and topography, and reflects both vertically averaged velocity structure in the upper mantle (from the SS leg) and low spherical harmonic degree structure in the lower mantle (from the S leg). (*b*) is constructed from the same data but is corrected for the traversal of the S leg through the lower mantle structure of model SH8/U4L8. (*b*) should represent vertically integrated upper mantle velocity structure, and fits a cooling halfspace velocity model of the oceanic crust better than (*a*).

arrival angles. This is particularly true for low orbit wave trains which are of most interest since the polarization of the later orbits becomes more and more insensitive to structure of odd harmonic degree (Woodhouse & Wong 1986). Polarization data have been collected for 150 selected events recorded by the global GEOSCOPE and IDA networks (a preliminary data-set was presented in Laske *et al.* (1994)).

A joint inversion of the phase and polarization data for a phase velocity map expanded up to $\ell = 16$ is shown in figure 6. The phase data do not require shorter wavelength structure (for example, no significant additional variance reduction is obtained by going from $\ell = 12$ to $\ell = 16$), but the polarization data are much better fit if shorter wavelength structure is added. Figure 7 uses a checkerboard test ($\ell = 14$) to demonstrate the tremendous improvement in short-wavelength resolution when polarization data are included in the inversion. A more detailed description of the data and the final phase velocity maps is given in Laske & Masters (1996). The final Love wave phase velocity maps are presented in figure 8 and show a strong

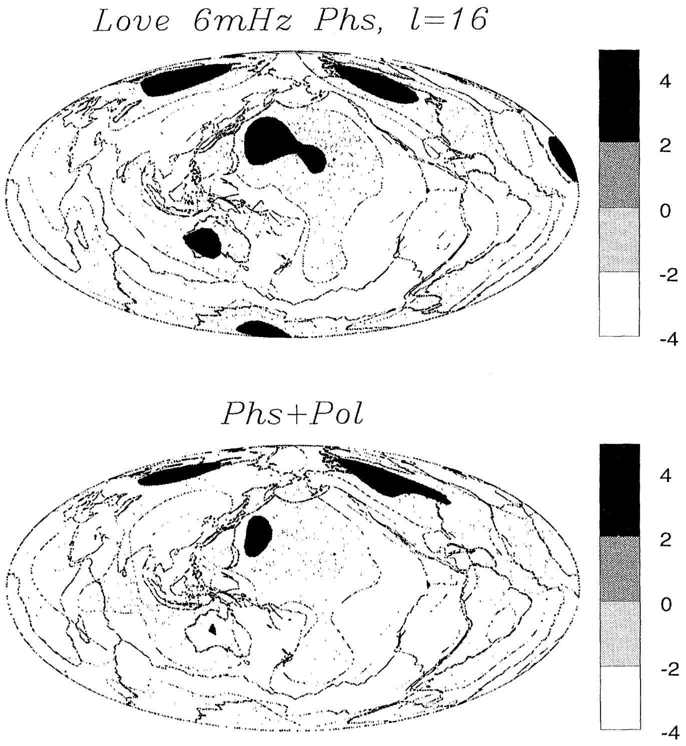

Figure 6. Comparison of the phase velocity maps obtained for Love waves at 6 mHz. For the upper map, only phase data were used for the inversion, while phase and polarization data were used to obtain the lower map. The maps are expanded in spherical harmonics up to degree $\ell = 16$ and show phase velocity perturbation in %. The phase data do not require structure above $\ell = 12$ but the fit of the polarization data can be dramatically improved by low amplitude structure between $\ell = 12$ and 16.

correlation with surface tectonics. It turns out that these data are critical for resolving upper-mantle shear velocity variations.

(*d*) *Mode structure coefficients*

The free oscillation data consist of 2034 structure coefficient estimates obtained from the studies of Smith & Masters (1989), Smith (1989), and Ritzwoller *et al.* (1986, 1988). We use structure coefficients up to harmonic degree 8 for 69 spheroidal modes. The data-set consists primarily of fundamental modes though there are 19 spheroidal overtones which are sensitive to lower-mantle structure. Details of the methods used for obtaining the structure coefficient estimates can be found in the original papers.

It should be noted that the structure coefficients for surface-wave equivalent modes and coefficients in the expansion of phase velocity maps are not independent data. Indeed, for large harmonic degree, we can convert the mode structure coefficients to an effective phase velocity map at the period of the mode though, because the mode coefficients are estimated using a standing wave analysis, there is no sensitivity to structure of odd harmonic degree (Jordan 1978*a*). Figure 9 shows the comparison of such a conversion with the even part of the phase–velocity map determined using surface-wave techniques by Laske & Masters (1996). It is remarkable that such

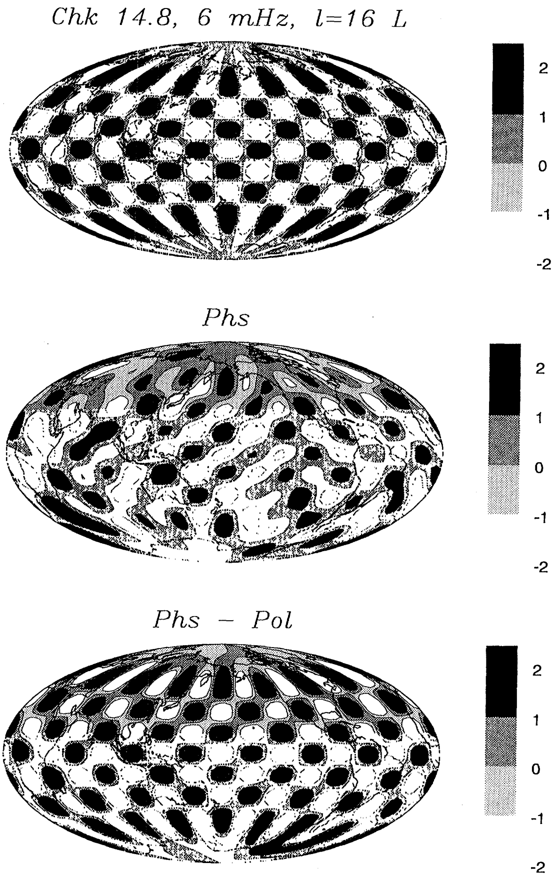

Figure 7. Resolution test using a Y_{14}^{8} checkerboard pattern (top panel). This test assumes that nonlinear effects are unimportant and inverts a synthetic data-set using the same operator that was used to invert the real data. The middle panel shows the recovery of the pattern when only phase data are included. The lower panel shows the recovery when phase and polarization data are used simultaneously in the inversion.

different analysis techniques give such similar answers which gives us confidence in both data-sets.

(*e*) *Spectral content of the data-sets*

Inspection of figures 3, 4, 5 and 8 shows that the data-sets are dominated by signals with long wavelength. This is made more obvious if we plot the amplitude spectra of the data (figure 10). The amplitude spectra for the travel time data-sets are estimated by performing a spherical spline fit to the cap values shown in figures 4 and 5 (Parker 1994, ch. 2) and then computing the equivalent spherical harmonic expansion of the splined field. This procedure penalizes short wavelength structure but the amplitude spectra up to about degree 10 are insensitive to the degree of smoothing used in the spline fitting. In every case, we find that long-wavelength structure dominates the data-sets and, in fact, most of the observed power is at harmonic degrees below 6. This observation is the primary motivation for parametrizing our shear-wave velocity structure in terms of spherical harmonics as they are likely to be an efficient basis for representing the dominant structure in the mantle.

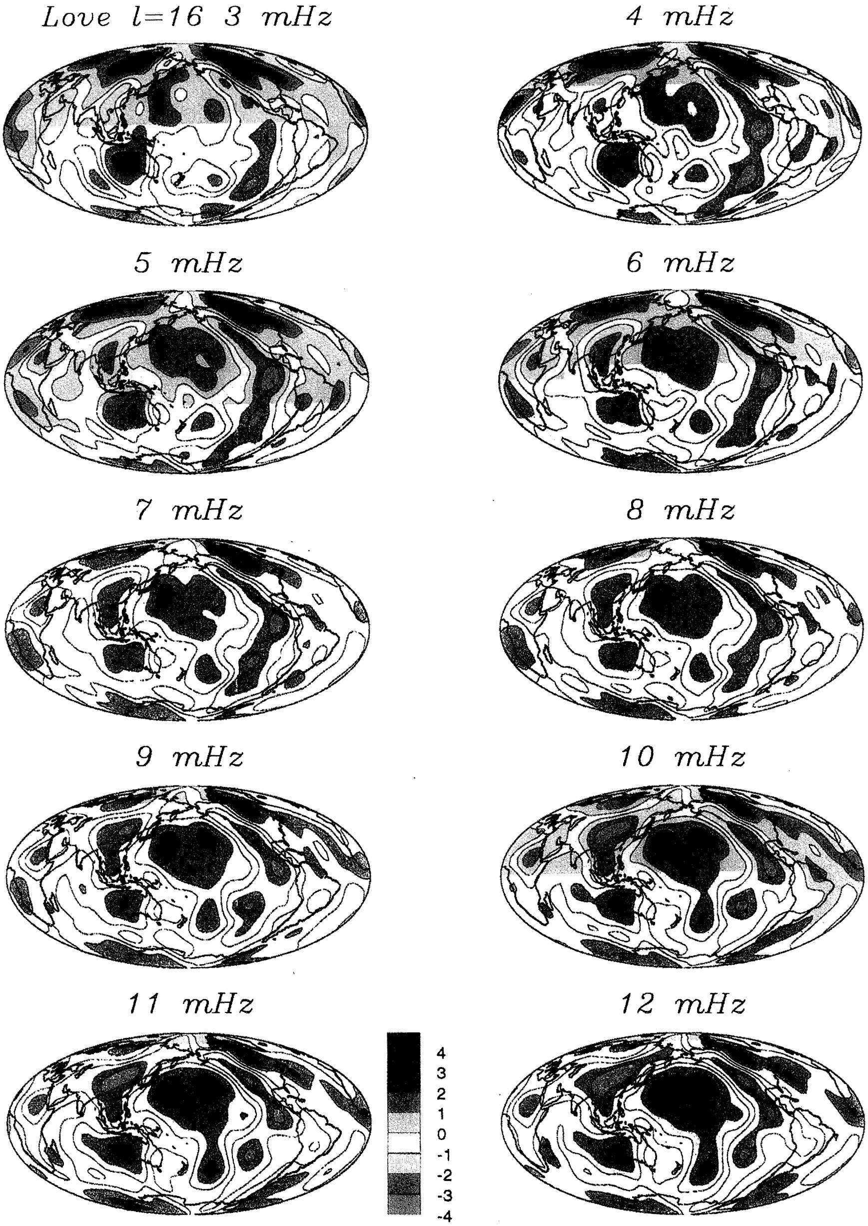

Figure 8. The ten Love wave phase velocity maps obtained from a smoothed inversion of phase and polarization data. The maps are expanded in spherical harmonics up to degree $\ell = 16$ and show phase velocity perturbation in %. The errors vary geographically and with frequency but do not exceed 0.3%.

3. Inversion

(a) *Parametrization*

One of our early inversions of the data used only $SS - S$ differential travel-time residuals in conjunction with a subset of the mode structure coefficients to invert for upper mantle structure (Woodward & Masters 1992). This work demonstrated

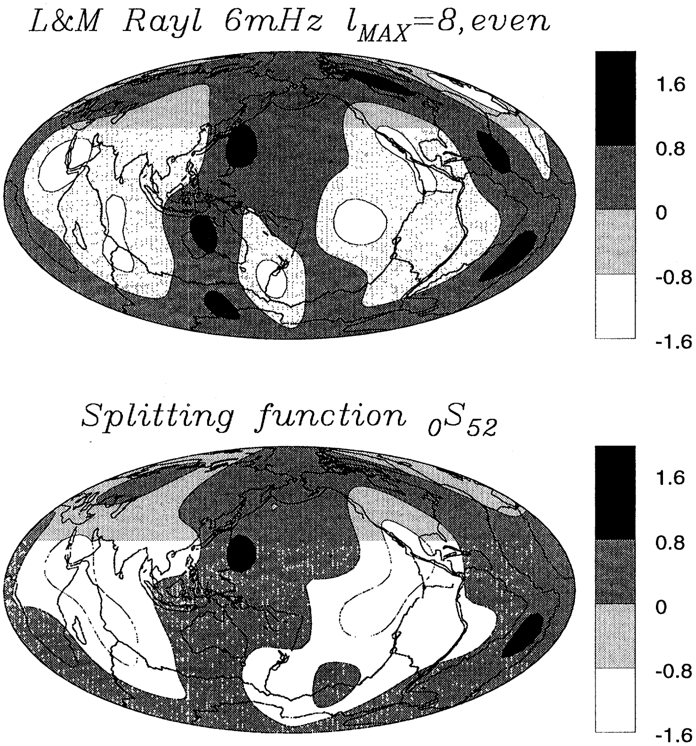

Figure 9. Comparison of the phase velocity map for Rayleigh waves at 6 mHz and the splitting function of spheroidal fundamental mode ${}_0S_{52}$. Since the splitting function is expanded only up to $\ell = 8$, the phase velocity map was truncated at $\ell = 8$ and only even harmonic degrees are shown.

that simple models can be constructed that go a long way to simultaneously fitting both data-sets but it also showed that there is a significant contribution to the $SS - S$ data from the lower mantle. Now that we also have extensive data-sets of S and $ScS - S$ times, an inversion for whole mantle structure is both feasible and desirable. Several preliminary inversions have been done (Masters & Bolton 1991) which initially followed Tanimoto (1990) and divided the mantle into eleven shells in each of which structure up to harmonic degree 10 was allowed. In our latest inversions, the model is parametrized in radius by natural cubic B-splines. We prefer these basis functions to the Legendre or Chebyshev polynomials used in other studies since these latter basis functions have global support and are capable of mapping structure in one part of the mantle to another. The cubic B-splines are the functions defined at a set of knots with continuous zeroth, first and second derivatives and with the minimum support (and with zero second derivatives at the end knots). The knots have been set at approximately 100 km spacing across the entire mantle, which clearly constitutes a radial overparametrization based on *a posteriori* evaluations of resolution (see below). This overparametrization and consistent knot spacing is desirable in mitigating the effects of a rather arbitrary choice of basis functions on the appearance of the resulting model. The shear velocity perturbation can now be written as

$$\delta v(r,\theta,\phi) = \sum_{l=1}^{16} \sum_{m=-l}^{+l} \sum_{k=1}^{30} {}_k\delta v_l^m b_k(r) Y_l^m(\theta,\phi),$$

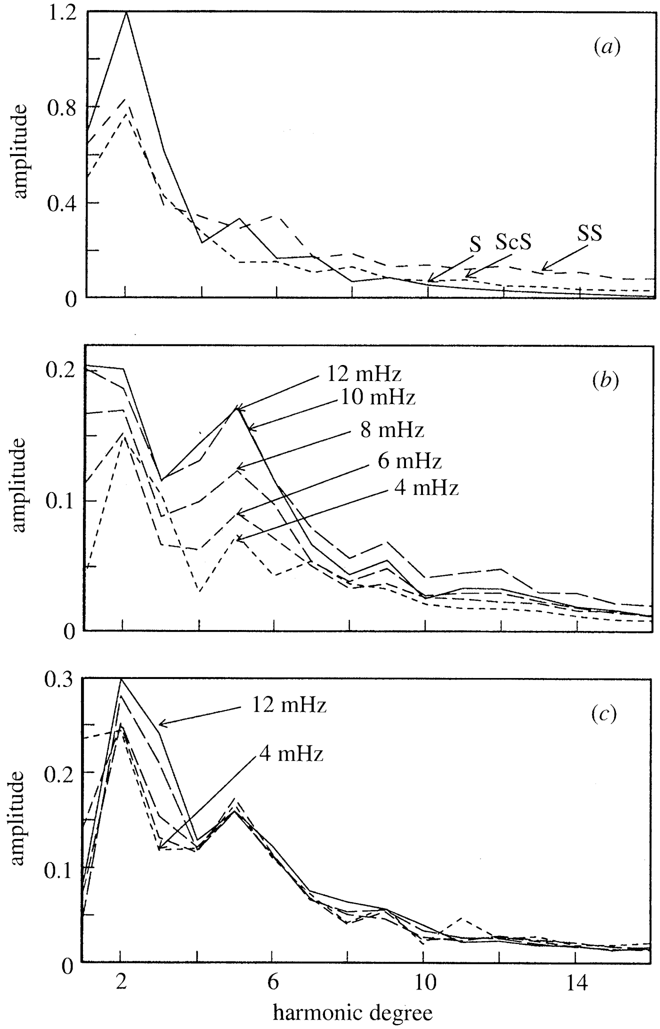

Figure 10. Amplitude spectra of the data-sets used in this study (e.g. figures 3, 4, 5, 8). The upper panel shows the spectra of the body wave travel times S, $SS-S$ and $ScS-S$ while the lower two panels are the spectra of the phase velocity maps for Rayleigh and Love waves at frequencies 4, 6, 8, 10 and 12 mHz. In all data-sets, the long-wavelength component ($\ell = 6$ and below) is clearly dominant.

where b_k is a B-spline and Y_l^m is a fully normalized surface spherical harmonic (see Edmonds 1960). The present experiments ignore the possibility of lateral variations in the topography of internal discontinuities. The travel time data we use are rather insensitive to the location of discontinuities. On the other hand, it was shown by Masters *et al.* (1982) that the long-period mode and surface-wave data are somewhat sensitive to the topography of mantle discontinuities giving a trade-off with structure in the immediate vicinity of the boundary. The experiments of Woodward & Masters (1992) suggest that this trade-off is not strong and that the boundary perturbations are only weakly constrained with the current data-sets. The constraints from the stacking of mantle discontinuity phases (Shearer & Masters 1992) can be included in the inversions and should help greatly in reducing these trade-offs. This will be the subject of future work.

One final point is that the crust has a significant impact on most of the data-sets but, at the same time, is too thin to be resolved by them. Most authors have handled this by applying a crustal correction to the data before inversion. We follow this procedure though it must be recognized that crustal structure is poorly known in many parts of the world and our correction may be quite uncertain. To compute the crustal corrections, we use the model of W. Mooney (personal communication, 1994) which is based on the work of Christensen & Mooney (1995). This model is a seven layer model (including water and ice) for v_p and ρ, compiled for 52 crustal types. Except for water and ice, an average Poisson's ratio of 0.27 is taken to compute v_s. Topography and bathymetry data are taken from the ETOPO5 database (National Geophysical Data Center 1986). The crustal model used in earlier works included the compilation of crustal thickness by Soller *et al.* (1982). Though our new crustal model is fairly detailed compared with the old one, it gives rather similar effects. As is well-known, the crustal correction actually increases the variance in most of the data-sets leading to larger amplitude velocity perturbations in the uppermost mantle.

(*b*) *Model construction*

The inverse solution is obtained following the philosophy espoused by Shaw & Orcutt (1985) and Constable *et al.* (1987). The aim of this method is to obtain a solution which minimizes the misfit, to within a prescribed tolerance, while simultaneously minimizing a measure of roughness of the model produced.

In matrix notation, our forward problem is

$$\boldsymbol{d} = \boldsymbol{G}\boldsymbol{m},$$

where $\boldsymbol{m}$ is the model of spherical harmonic expansion coefficients. For the travel time data, $\boldsymbol{d}$ is a vector of travel time residuals and the corresponding rows of $\boldsymbol{G}$ are computed using the linearized theory given by Dziewonski (1984). The theoretical basis for this interpretation of the travel time data is rather simplistic as it is based on ray theory and invokes Fermat's principle to justify the neglect of perturbations in ray paths from those in the spherically averaged Earth. Grand (1994) has shown that ray-path deviations can be quite severe for rays which bottom in the upper mantle, particularly in the presence of low-velocity zones. All of our travel time data bottom in the lower mantle and '*a posteriori*' ray-tracing experiments indicate that ray-path deviations are small and have almost no effect on the predicted travel time (Michael Kendall, personal communication). For the mode and phase-velocity data, $\boldsymbol{d}$ is a vector of structure coefficients or phase-velocity expansion coefficients and the corresponding rows of the matrix $\boldsymbol{G}$ are computed using the results of Woodhouse & Dahlen (1978). In reality, the travel-time data (in particular, the absolute S times) are sensitive to the event location as well as to the velocity structure. We therefore use a projection algorithm to find linear combinations of all the travel-time data for a particular event which are, to first order, insensitive to the event location. Such techniques are quite common in tomographic analyses (see Scott *et al.* 1994) but it turns out that the velocity models that we obtain do not change much if we omit this step.

We desire a model such that the misfit is of a predicted size. That is, we want

$$\|\boldsymbol{d} - \boldsymbol{G}\boldsymbol{m}\|^2 = \chi^2,$$

where χ^2 is an estimate of the expected misfit in the data and $\|\cdot\|$ is the Euclidean norm. By normalizing the rows of $\boldsymbol{d}$ and $\boldsymbol{G}$ by the estimated errors of the individual data, χ^2 should be roughly the same as the number of data used. We also desire that the model be smooth, which is ensured by penalizing a measure of roughness,

$$\|\partial \boldsymbol{m}\|^2,$$

where ∂ could, for example, be the first or second differencing operator. A solution which satisfies these constraints can be obtained by using Lagrange multipliers (Constable *et al.* 1987). The role of the Lagrange multiplier, μ, is illustrated by the resulting normal equation,

$$[\boldsymbol{G}^{\mathrm{T}}\boldsymbol{G} + \mu\partial^{\mathrm{T}}\partial]\boldsymbol{m} = \boldsymbol{G}^{\mathrm{T}}\boldsymbol{d}.$$

Solving this equation for $\mu = 0$ gives us the best fitting (least squares) solution, but there is no penalty for roughness and the data may well be overfit. As μ is increased the penalty for roughness increases, so the solution is smoother but the misfit is greater. In practice, we look at a family of solutions for a variety of Lagrange multipliers and choose a compromise in the trade-off between roughness and misfit. Although the errors are difficult to establish in an *a priori* fashion, conservative error estimates from the analysis of the data are used to select models with a reasonable misfit to the data. In the interest of increased numerical stability over a wide range of Lagrange multipliers and smoothing matrix constructions a factored form of the normal equations is solved by the QR method (see Parker 1994).

The construction of the smoothing operator is complicated by the fact that we usually wish to treat radial and lateral smoothing of the model differently (since the natural length scales and resolution of the data can be quite different in the radial and lateral directions). We follow Woodward & Masters (1992) and separate the smoothing of lateral and radial variations by writing

$$\partial^{\mathrm{T}}\partial = \boldsymbol{D} = \boldsymbol{D}_{\mathrm{L}} + \alpha\boldsymbol{D}_{\mathrm{R}}.$$

$\boldsymbol{D}_{\mathrm{L}}$ controls lateral smoothing and $\boldsymbol{D}_{\mathrm{R}}$ controls radial smoothing; α is merely an empirically determined weighting factor which is used to balance the radial and lateral smoothness. Lateral roughness (for each radial basis function) can be expressed as

$$\int_{\Omega} |\nabla_1^2 \delta v_k(\theta,\phi)|^2 \,\mathrm{d}\Omega,$$

where $\delta v_k = \sum_{l,m} {}_k\delta v_l^m Y_l^m(\theta,\phi)$, ∇_1^2 is the surface Laplacian and Ω is the surface of the sphere. It therefore follows that a total measure of lateral roughness of the model can be written:

$$\boldsymbol{m}^{\mathrm{T}}\boldsymbol{D}_{\mathrm{L}}\boldsymbol{m} = \sum_{k,l,m} l^2(l+1)^2 |{}_k\delta v_l^m|^2,$$

Thus $\boldsymbol{D}_{\mathrm{L}}$ is a diagonal matrix with terms of the form $l^2(l+1)^2$ along the diagonal.

Radially, we again use a second derivative measure of roughness so that the total radial roughness of the model is written:

$$\boldsymbol{m}^{\mathrm{T}}\boldsymbol{D}_{\mathrm{R}}\boldsymbol{m} = \sum_{l,m}\int_c^a \left|\sum_k {}_k\delta v_l^m \frac{\partial^2}{\partial r^2} b_k(r)\right|^2 \mathrm{d}r,$$

where c is the core–mantle boundary radius and a is the radius of the base of the crust.

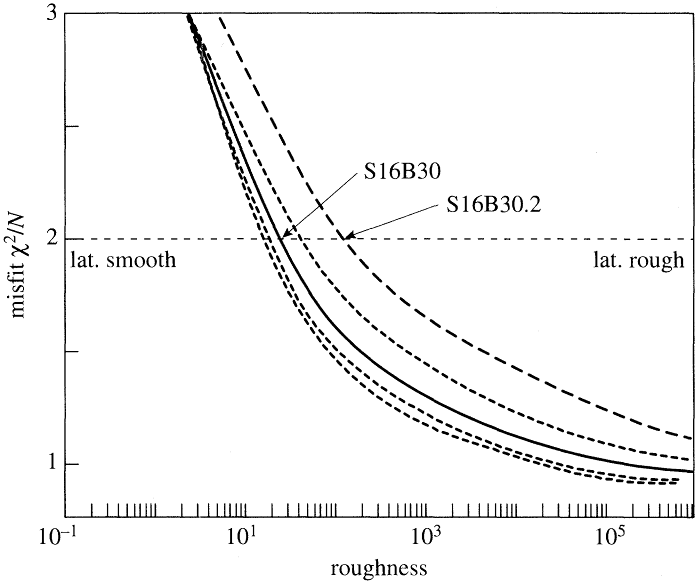

Figure 11. Trade-off curves from the inversions for S16B30. A total data misfit level of $\chi^2/N = 2.0$ lies at the dashed line; models below this line are rougher, and models above smoother. The family of curves is generated with a range of values of the parameter α (see text). At a given misfit, models on the solid curve (e.g. S16B30) are radially rougher and laterally smoother than models on the dashed curves to the right (e.g. S16B30.2).

The inversion is now done for a variety of values of α and the resulting trade-off curves are shown in figure 11. We find that there is a range of models which give acceptable fits to the data but vary in their smoothness characteristics. Choosing a particular value for the combined misfit of all data-sets yields a range of misfits for each of the data-sets. In the case of choosing a combined misfit χ^2/N of 1.0 the Rayleigh and Love wave data-sets are overfit at χ^2/N of 0.45 and 0.85, respectively. In the interest of choosing a conservative model (i.e. not unnecessarily rough), models with a combined misfit of 2.0 are deemed preferable. The range of misfits for each of the data subsets is shown in figure 12. We present two models in figures 13 and 14 which both fit the data at the combined misfit level of 2.0. The model in figure 13 is laterally very smooth but radially rough while the other one is laterally rougher but radially smoother (figure 14). The gross features of the models are similar with large-amplitude structure near the top and bottom of the mantle and with lower-amplitude structure in the mid mantle. Small-scale features are, however, quite different. Our prejudice for the model in figure 13 is founded on considerations of figure 12 and supported by the comparison of small scale structure in the model with small scale structure in the primary data-sets. Models less laterally rough (smaller α) are a poorer fit to the Love wave data-set, and models radially smoother (larger α) are a poorer fit to the Rayleigh wave and spheroidal mode data. A reasonable compromise is to choose the model which satisifies all the data-sets fairly well. The spectrum of lateral variations in the ScS-S data-set is also more consistent with the model in figure 13 suggesting that this model is reasonable throughout the mantle.

Figure 13, therefore, shows our 'best' model (S16B30) and, for comparison, model SH12WM13 of Su *et al.* (1994) is plotted in figure 15. In figure 16, we show the root mean square (RMS) amplitude as a function of depth of both models along with the

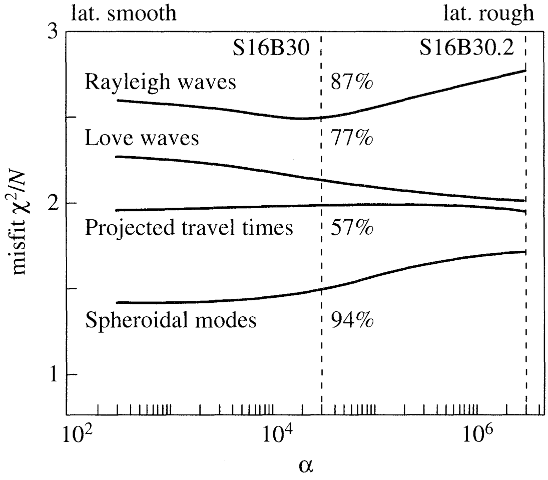

Figure 12. Misfit to various data-sets for models with a total misfit of $\chi^2/N = 2.0$. Sampling along the trade-off curves in figure 11 with this misfit yields a set of models with varying smoothness characteristics. These models fit the subsets of the data differently, presumably according to how inconsistent the smoothing constraint is with the structure preferred by the data subset. The vertical line corresponds to the value of α of S16B30, and is chosen to satisfy the surface wave and mode data-sets generally the best. Variance reductions using model S16B30 are 57% for travel times and 77-94% for the surface waves and spheroidal modes.

correlation between them. S16B30 is larger in amplitude near both boundaries of the mantle but both models correlate well in shape in these regions. The correlation is poorest in the mid-mantle, where structure is of low amplitude, but the correlation is significant at the 95% level (which is about 0.3 for this number of parameters). We believe that our model exhibits higher amplitudes near the core–mantle boundary because of the inclusion of the data-set of absolute S times which sample this region. Such data are absent from SH12WM13 though recent models by the Harvard group which include $SKS - S$ differential times have amplitudes similar to S16B30 (Adam Dziewonski, personal communication). The reason that S16B30 has larger amplitude structure near the surface is less clear though we believe it to be necessary to explain the short-period Love wave data of figure 8.

(*c*) *Resolution and error analysis*

We evaluate the resolution of the modelling algorithm by performing several different inversion experiments using the operator which produced the model from the real data. This operator was applied to synthetic data-sets constructed from models consisting of checkerboard patterns of approximately 250 km thickness placed at various levels in the mantle. This technique allows depth resolution as well as lateral resolution to be evaluated. The results for three layers are shown in figure 17 for a pattern which is a Y_7^4 spherical harmonic. Since most of the power in the model in figure 13 is of lower harmonic degree, the results of this test may be somewhat pessimistic. When the pattern is placed in the upper mantle (figure 17*c*), the inversion smears the answer in depth a little (upper panel) but recovers the geographic pattern very well (lower panel). Our data are actually capable of accurately recovering harmonic patterns up to degree 16 in this region. In the mid and lower mantle (figures 17*a*, *b*) the pattern is recovered well in the Northern Hemisphere but reveals the effects of sampling inadequacies in the Southern Hemisphere. The recovered patterns tend to

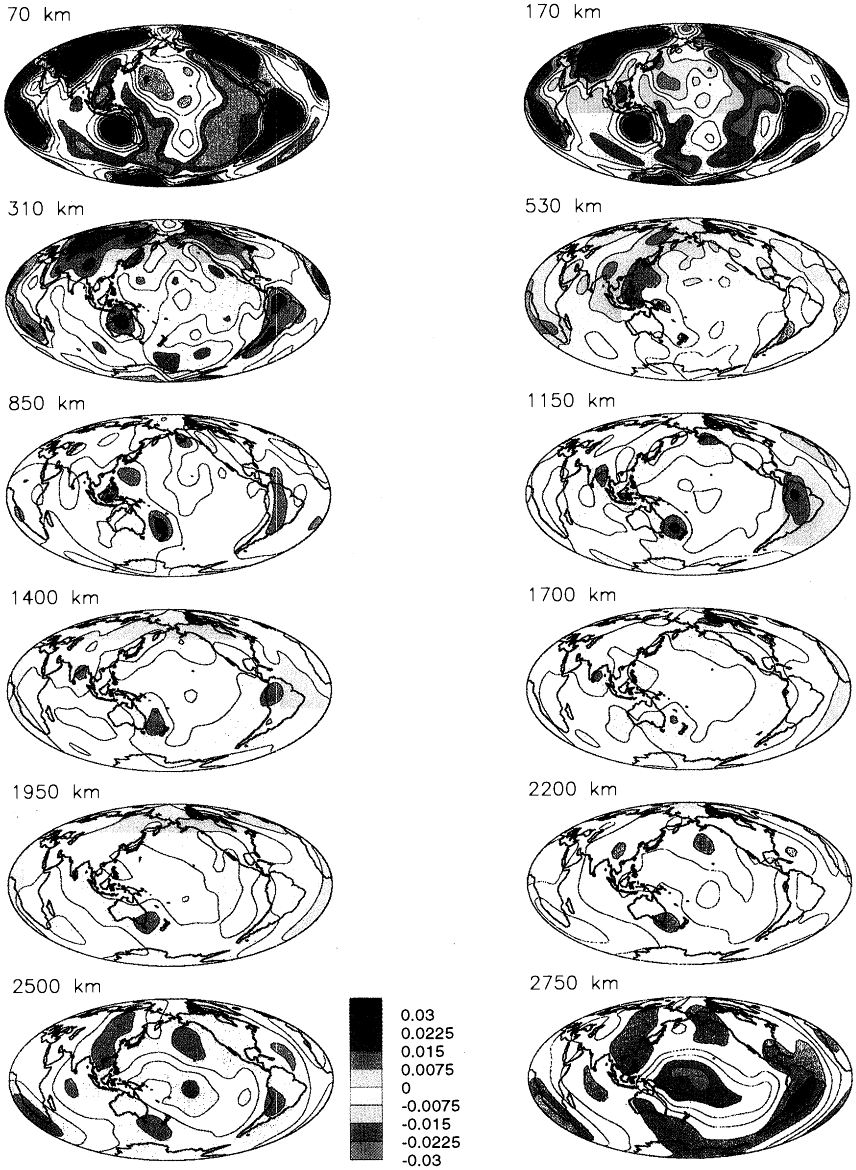

Figure 13. Twelve depth slices of model S16B30. Contoured values are shear velocity perturbation relative to the global model average at a given depth.

have low amplitudes where resolution is poor so the total RMS amplitude of the map is underestimated. On the other hand, where resolution is good, the peak values are quite close to the input values.

In all cases, sharp radial features are smeared 150–250 km in depth with some low amplitude contamination spreading across the lower mantle. This may, in part, be due to the second derivative smoothing which strongly penalizes sharp changes with

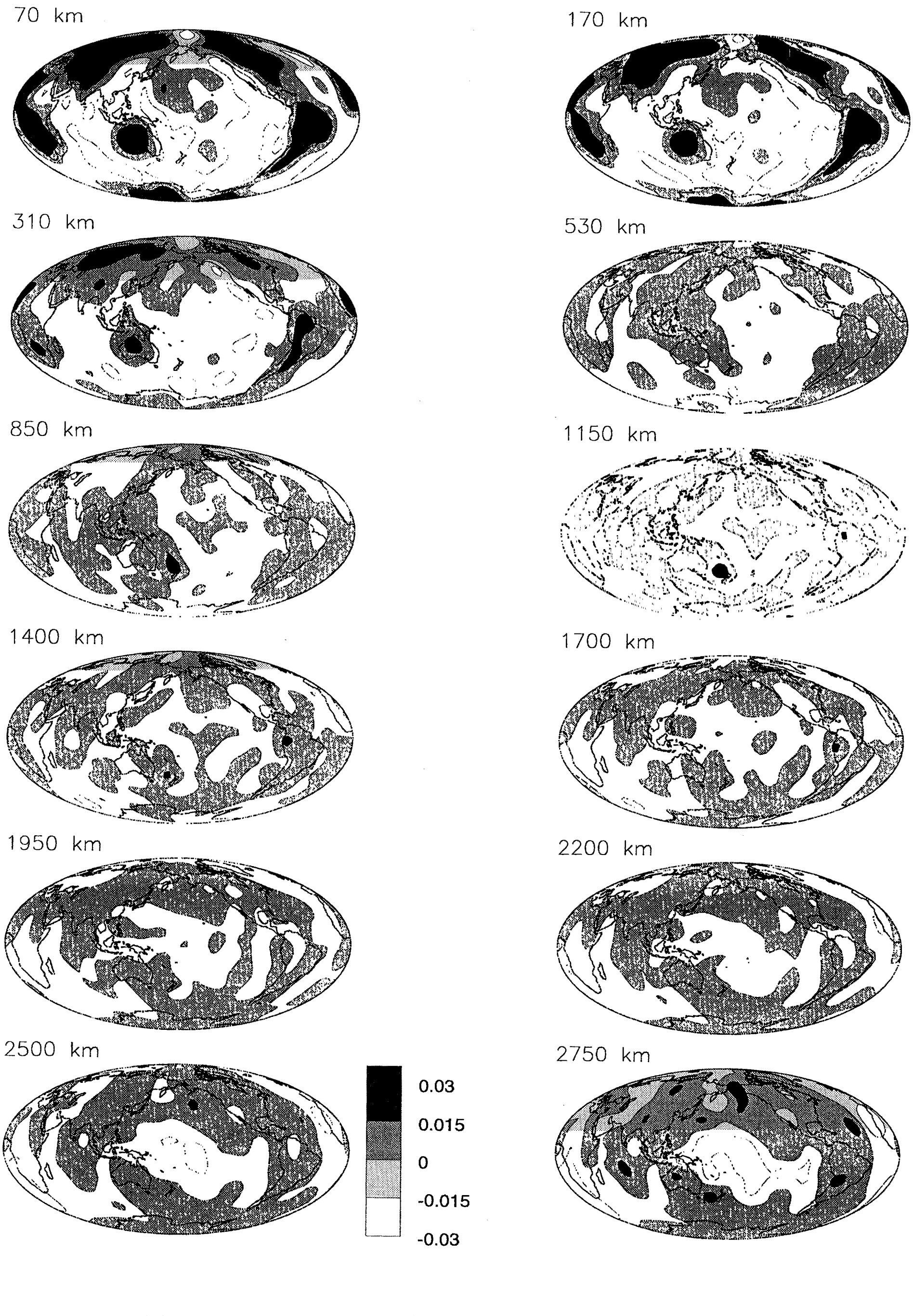

Figure 14. Model S16B30.2, plotted as in figure 13. While radially smoother than S16B30 (figure 13), this model is laterally rougher, as is especially evident in the comparison of the lower mantle slices of figures 13 and 14. Even though the total data misfit expresses no preference for model S16B30 against S16B30.2, it is argued that S16B30 is a better compromise amongst the misfits shown in figure 12, and that S16B30.2 posseses spurious structure when compared to data sets such as $ScS - S$.

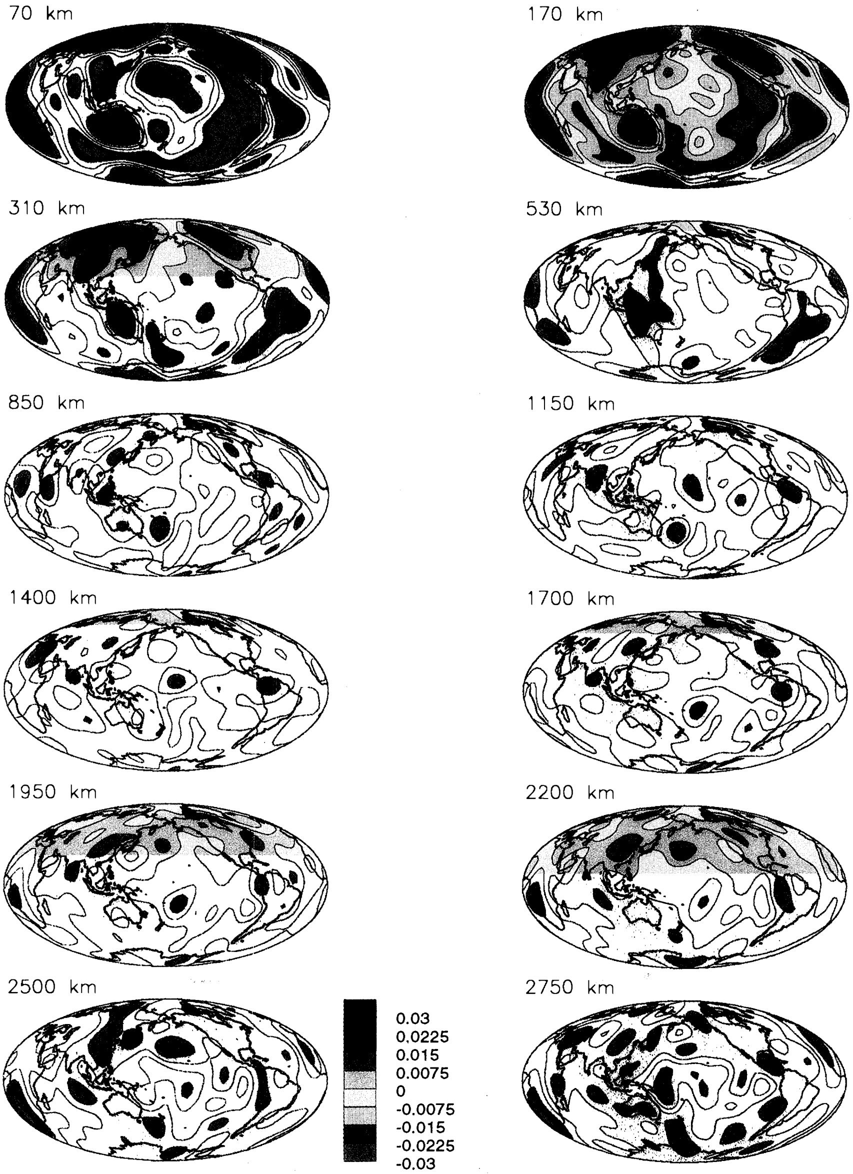

Figure 15. Model SH12WM13 plotted as in figure 13. All the models presented here have a relatively small fraction of data in common (part of the $SS-S$ and $ScS-S$ data-sets), but were obtained by different methods and employ different radial basis functions. The main differences between S16B30 (figure 13) and SH12WM13 are in the patterns of mid-mantle structure and in the size of anomalies in the lowermost mantle.

radius and we are currently experimenting with different radial smoothing criteria to see if we can reduce radial leakage.

Maps of model variance are computed using a Monte-Carlo technique by applying the matrix inversion algorithm to several hundred randomly chosen realizations of the data errors. Model variances can also be obtained by forming the covariance

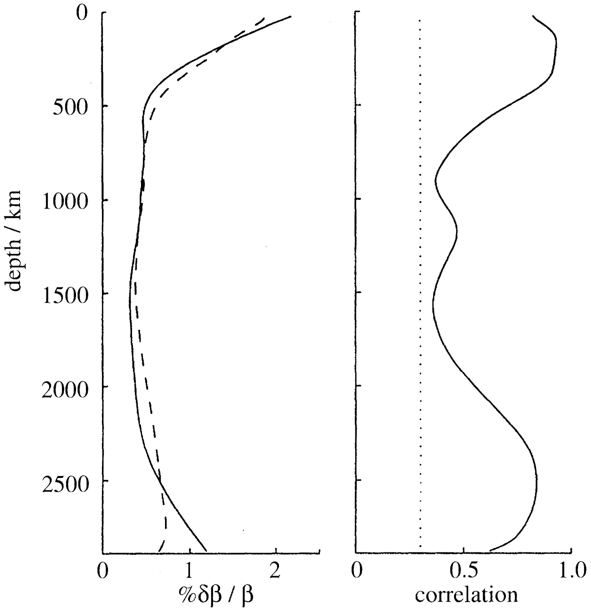

Figure 16. Comparison of S16B30 and SH12WM13 as a function of depth. The left panel shows the RMS amplitude as a function of depth (S16B30 is the solid line). The main difference between the two models occurs near the base of the mantle and is probably due to the inclusion of absolute S travel times in the inversion for S16B30. The right panel shows the cross-correlation between the models as a function of depth (computed for spherical harmonics up to degree 12). The dotted line indicates the 95% significance level (about 0.3).

matrix of the model parameters and propagating errors from the data to errors in the model, but it turns out to be computationally easier to use the Monte-Carlo technique given the size of the matrices we have to deal with. Errors are largest near the boundaries of the mantle but peak at about 0.2% (more than a factor of ten smaller than the peak signal). In the mid-mantle, formal errors are about 0.1%, which, again, is much smaller than the model there. Scaling up the errors by a factor of $\sqrt{2.0}$ to account for the fact that our data are not perfectly fit by the models doesn't change the conclusion that most of the detail in the models is formally above the noise.

4. Discussion

Our final model, S16B30, is shown in figure 13 and four cross-sections are shown in figure 18. The model is characterized by large-amplitude, large-scale structure, peaking at about ±6% in the upper mantle and at about ±2.5% at the base of the mantle. The RMS amplitude of velocity perturbation as a function of depth changes smoothly from high amplitudes near the surface to low amplitudes from 500–2200 km depth to higher amplitudes near the core mantle boundary (CMB). Structure shallower than 300–400 km has peak amplitudes in spherical harmonic degrees 1, 4 and 5 while degree 2 is predominant in the transition zone. The spectra in the mid mantle are whiter though, below about 2000 km depth, the lower mantle is again dominated by degree 2 structure.

Structure in the uppermost and lowermost mantle appears to be the best es-

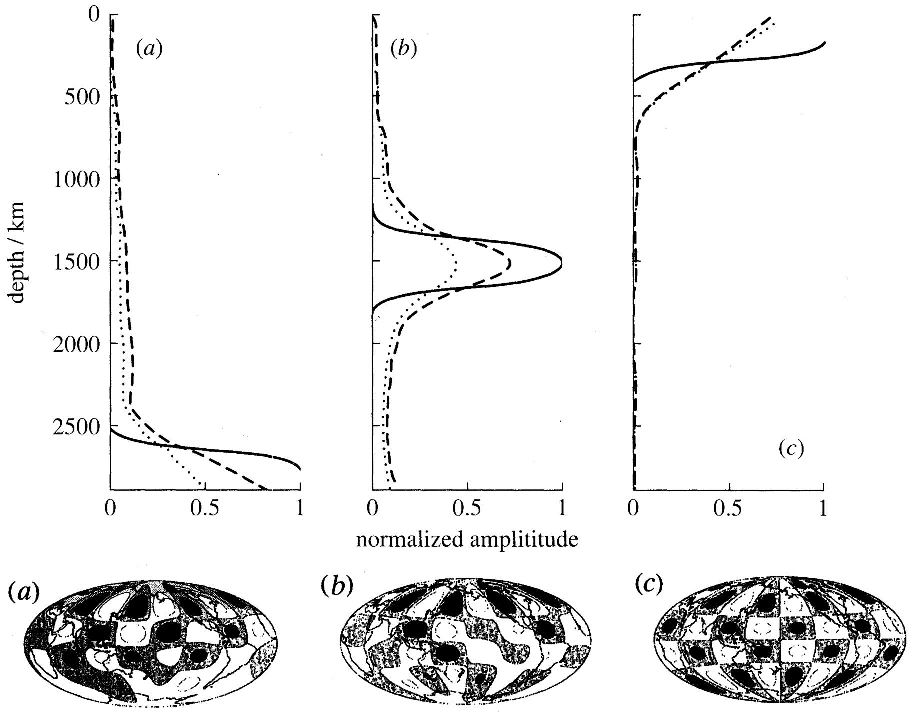

Figure 17. Attempts to recover checkerboard patterns at three levels in the mantle. The input pattern is the linear combination of three natural B-splines in radius and is a Y_7^4 spherical harmonic laterally. The solid curve in the upper plots is the amplitude against depth of the input pattern, normalized to have a peak value of 1. The dashed line is the peak recovered value at each depth as a fraction of the input pattern peak at that depth. The dotted line is the fraction of the RMS amplitude recovered. The lower plots show the recovered pattern at the depth of the peak recovered RMS. Although not shown, the input pattern is essentially identical to the recovered pattern in (*c*). (*a*) An attempt to recover a checkerboard pattern situated at the bottom of the mantle (the bottom three B-splines). Although some of the input pattern is smeared into low amplitudes across the lower mantle, the radial resolution is taken to be the increase in radial extent of the main peak of the recovered pattern which is roughly 200 km. The difference in the fraction of recovered RMS and peak amplitudes is due to the geographic variation of the resolution. (*b*) An attempt to recover a checkerboard pattern situated in the mid-mantle. As in (*a*), the input pattern is the linear combination of three B-splines in radius. The edges of the input peak are smeared 200–300 km radially. (*c*) Attempt to recover a checkerboard pattern situated in the upper mantle. The model construction algorithm tends to smear the anomaly about 200 km radially although the shape is very well-recovered.

tablished, presumably because of its high amplitude and red spectrum. The cross sections reveal low velocity anomalies along mid-ocean ridges extending in some cases to at least 300 km depth. The effects of the cooling oceanic lithosphere are evident in the shallow model structure in oceanic regions. Fast regions extend 300–400 km beneath continents, supporting Jordan's (1978*b*) hypothesis of a continental tectosphere. Backarc regions are characterized by shallow low velocities. In the lower mantle, a ring of high velocity surrounds the Pacific and large slow regions are present in the Central Pacific and beneath Africa. Although SH12WM13 and S16B30 are less similar in the transition zone, both show fast regions beneath the subduction zones in the western Pacific and beneath South America.

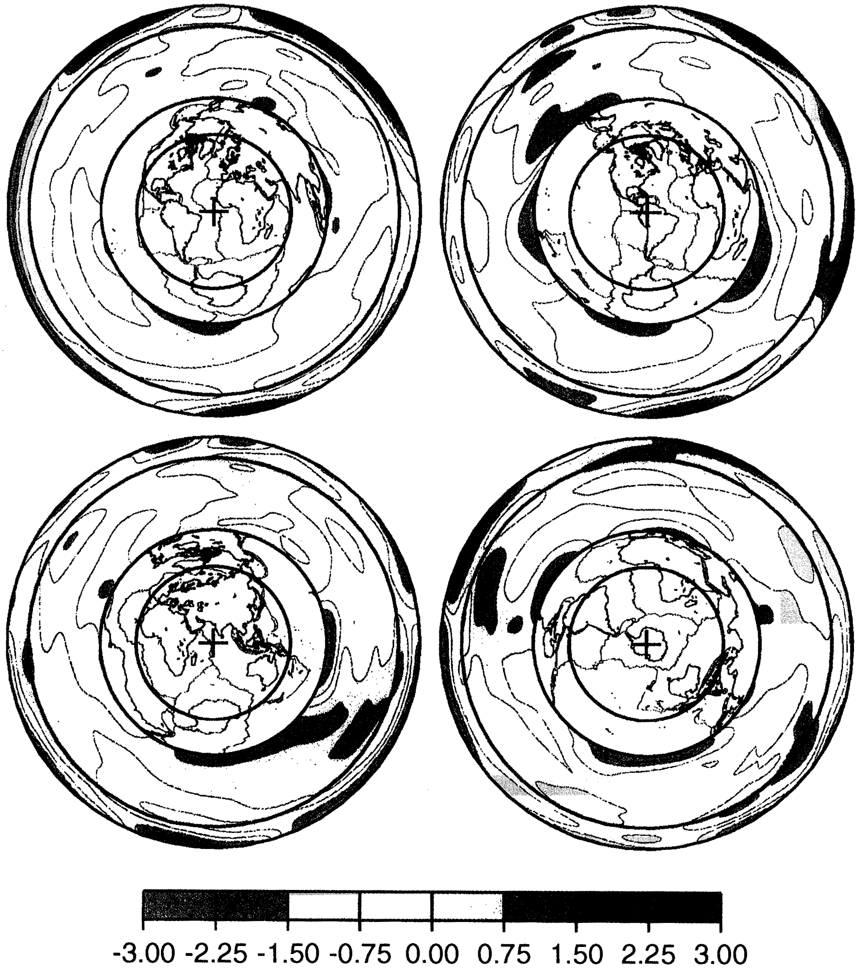

Figure 18. Cross-sections through model S16B30. The shear velocity perturbation relative to the model average at depth is contoured. The slices intersect the surface along the great circles plotted on azimuthal equidistant projections in the centres of the cross sections.

The resolution tests (figure 17) and comparison of SH12WM13 and S16B30 show that interpretation of features in the mid-mantle is more dubious. Resolution is strongly a function of geographic location, with the highest resolution in the circum-Pacific and Asian regions. We should also bear in mind that radial smearing of short wavelength structure is more severe than for long wavelengths and so is likely to be more of a problem in this region. Figure 13 and the cross sections show several more or less radially continuous fast features. Examples are beneath the Tasman Sea, India, the North Central Pacific, and South America, all regions which may well have been supplied with downgoing material in the past (Ricard *et al.* 1994). All of these features are in regions of fairly good lateral resolution (figure 17). Synthetic tests of convection simulations show that similarly sized cylindrical features which are oriented vertically in the mid-mantle can be resolved by tomography (Johnson *et al.* 1996) implying that we are on the verge of imaging some short-wavelength mid-mantle anomalies.

There appear to be several slow features extending through the mid mantle. The large slow feature beneath the Azores (figure 18) is the most notable and is in a moderately well-resolved region. Slow material also extends upward from the CMB beneath South Africa towards the mid-ocean ridge south of Africa. A generally slow, low amplitude region in the Central and Western Pacific connects the high amplitude slow anomalies at the CMB to the slow regions in the upper mantle. As stated above, resolution suffers greatly in the mid mantle in both the Central Pacific and beneath South Africa, so that these connections may be less (or more) substantial than they appear.

It is tempting to interpret the general features of the tomographic models in terms of the results of recent three-dimensional simulations of mantle convection. Such an interpretation is dangerous given the relatively simple rheologies used in most convection simulations (see Tackley *et al.* (1994) for a thorough discussion). For example, we might attribute the dominance of low spherical harmonic degree structure in the Earth (or, more precisely, the radial variation of power spectra) to the effects of the phase transition at 660 km depth (Tackley *et al.* 1993) though the presence of plates is likely to be at least as important. As discussed in Jordan *et al.* (1993), global diagnostics of mantle structure reveal major differences between the predictions of some three-dimensional convection simulations and mantle tomography. RMS amplitude of shear velocity and the radial correlation function (RCF) introduced in Jordan *et al.* (1993) are two simple diagnostics of interest. While three-dimensional numerical convection simulations modelling the effects of the 400 and 660 phase changes predict high RMS amplitudes across the upper mantle and a sharp decrease at the 660 discontinuity (Tackley *et al.* 1994), such a pattern is not evident in S16B30 (figure 16*a*). The cross-sections and figure 16*a* show that large-amplitude structure is confined to about the top 450 km in S16B30 and apparently does not extend significantly into the transition zone. This is also true of model SH12WM13 where structure extends a little deeper but is essentially confined above 500 km. We have shown (Johnson *et al.* 1996) that our tomographic methods should faithfully reproduce the change in RMS amplitude in the three-dimensional mantle convection simulation of Tackley *et al.* (1993) near the 660 discontinuity, suggesting that such a change in structure across the 660 does not exist in the Earth. The radial decorrelation in structure in the vicinity of the 660 in the RCF of this convection simulation was also shown to be well-recovered by the tomography, so the absence of such a feature in the RCF of S16B30 (figure 19) also supports the conclusion that phase transition at 660 km may not be the dominant controlling factor in the convection of the actual mantle. The RCF of S16B30 shows only a slight decorrelation at shallower depths, which may be related to the disappearance of continental roots.

5. Future directions

A comparison of models S16B30 and SH12WM13 suggests that mantle tomography has matured to the point where we can reliably recover the large-scale variation of shear velocity in the mantle. Clearly, neither model S16B30 nor model SH12WM13 is the final word in mantle tomography. Some improvement can be achieved simply by expanding the current data-sets to take advantage of the rapidly growing digital global seismic network. Many of the problems associated with imaging structure in the Southern Hemisphere of the lower mantle can be expected to be addressed in this way. We should also be including boundary perturbations in the inversions though

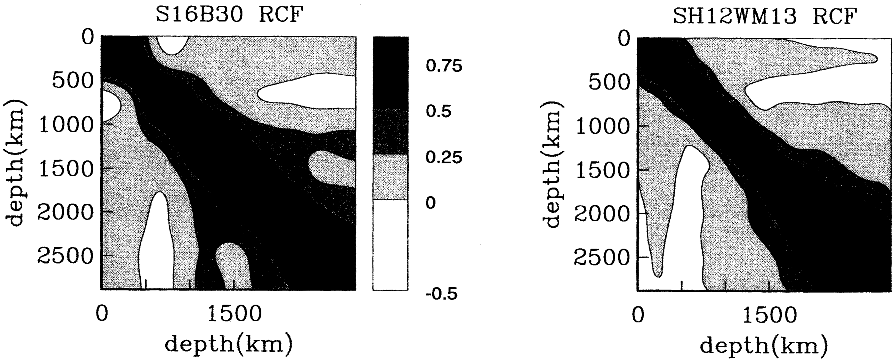

Figure 19. Radial correlation functions for models S16B30 and SH12WM13. These are contours of the cross-correlation between the model patterns on two spherical surfaces specified by the depths on the axes. The diagonal of the plot represents the correlation of model patterns at a given depth with themselves and therefore must have the value 1.0. If the model has similar structure in radius, the diagonal ridge will broaden, and vice versa. Recent numerical modelling of convection in a spherical shell suggests that the width of the diagonal correlation ridge with depth may provide some insight into the important factors in mantle convection. For example, neither of the RCFs for models S16B30 nor SH12WM13 have the narrowing of the correlation ridge predicted by numerical simulations of mantle convection with a phase change at the 670 km discontinuity.

these tend to be poorly resolved with the existing data (Woodward & Masters 1992). The addition of data-sets of conversions and reflections from mantle discontinuities (Shearer 1991*b*) should do much to help in this regard.

As the data-sets expand and extend to higher frequencies, we will be tempted to try and resolve finer and finer scale structure. This will force an evaluation of the rather simple theoretical techniques currently used to interpret the data. In particular, we still lack fast and/or accurate methods to calculate synthetic body wave and short-period surface wave seismograms for realistic three-dimensional models. We also need to properly incorporate attenuation into the inversions and we need to evaluate the importance of anisotropy on a global scale. While rapid progress is being made on many of these fronts, global seismology still has a long way to go.

This research has been funded by grants from the National Science Foundation. G.L. has been partly supported by the Green Foundation of La Jolla and S.J. has been partly supported by an IGPP/Los Alamos minigrant. The inversion computations were performed on an Intel Paragon parallel supercomputer at the San Diego Supercomputer Center using funds from the SIO block grant. We also thank the network operators (USGS, IDA, GEOSCOPE) for producing such high-quality data and the IRIS DMC for making the data so easy to access.

References

Bolton, H. & Masters, G. 1991 Long period absolute *P* times and lower mantle structure. *Eos* **72**, 339.

Christensen, N. I. & Mooney, W. D. 1995 Seismic velocity structure and the composition of the continental crust: a global view. *J. Geophys. Res.* **100**, 9761–9788.

Constable, S. C., Parker, R. L. & Constable, C. G. 1987 Occam's inversion: a practical algorithm for generating smooth models from electromagnetic sounding data. *Geophys.* **52**, 289–300.

Doornbos, D. J. 1983 Observable effects of the seismic absorption band in the Earth. *Geophys. Jl R. Astr. Soc.* **75**, 693–711.

Dziewonski, A. M. 1984 Mapping the lower mantle: determination of lateral heterogeneity in P velocity up to degree and order 6. *J. Geophys. Res.* **89**, 5929–5952.

Dziewonski, A. M. & Woodhouse, J. H. 1987 Global images of the Earth's interior. *Science* **236**, 37–48.

Edmonds, A. R. 1960 *Angular momentum and quantum mechanics.* Princeton University Press.

Forte, A. M., Dziewonski, A. M. & Woodward, R. L. 1993 Aspherical structure of the mantle, tectonic plate motions, nonhydrostatic geoid, and topography of the core–mantle boundary. In *Dynamics of the Earth's deep interior and Earth rotation* (Geophysical Monograph 72), IUGG vol. 12 (ed. J. -L. LeMouël, D. E. Smylie & T. Herring), pp. 135–166.

Grand, S. P. 1994 Mantle shear structure beneath the Americas and surrounding oceans. *J. Geophys. Res.* **99**, 11 591–11 621.

Hager, B. H. & Clayton, R. W. 1989 Constraints on the structure of mantle convection using seismic observations, flow models, and the geoid. In *Mantle convection* (ed. W. R. Peltier), pp. 657–763. New York: Gordon and Breach.

Inoue, H., Fukao, Y., Tanabe, K. & Ogata, Y. 1990 Whole mantle P-wave travel time tomography. *Phys. Earth Planet. Interiors* **59**, 294–328.

Johnson, S. G., Masters, G., Tackley, P. & Glatzmaier, G. A. 1996 How well can we resolve a convecting mantle? *J. Geophys. Res.* (Submitted)

Jordan, T. H. 1978*a* A procedure for estimating lateral variations from low-frequency eigenspectra data. *Geophys. Jl R. Astr. Soc.* **52**, 441–455.

Jordan, T. H. 1978*b* Composition and development of the continental tectosphere. *Nature* **274**, 544–548.

Jordan, T. H. & Lynn, W. S. 1974 A velocity anomaly in the lower mantle. *J. Geophys. Res.* **79**, 2679–2685.

Jordan, T. H., Puster, P., Glatzmaier, G. A. & Tackley, P. J. 1993 Comparisons of seismic earth structures and mantle flow models using radial correlation functions. *Science* **261**, 1427–1431.

Karato, S. 1993 Importance of anelasticity in the interpretation of seismic tomography. *Geophys. Res. Lett.* **20**, 1623–1626.

Laske, G. 1993 The frequency-dependent polarization of long-period surface waves and its implication for global phase velocity maps. Doctoral Thesis, Universität Karlsruhe, Germany.

Laske, G. & Masters, G. 1996 Constraints on global phase velocity maps by long-period polarization data. *J. Geophys. Res.* (In the press.)

Laske, G., Masters, G. & Zürn, W. 1994 Frequency dependent polarization measurements of long period surface waves and their implications for global phase velocity maps. *Phys. Earth Planet. Interiors* **84**, 111–137.

Masters, G. & Bolton, H. 1991 Large-scale shear velocity structure of the mantle. *Eos* **72**, 316.

Masters, G., Bolton, H. & Shearer, P. 1992 Large-scale 3-dimensional structure of the mantle. *Eos* **73**, 201.

Masters, G., Johnson, S. & Sheehan, A. F. 1993 $SS-S$ and the depth of shear velocity anomalies under ridges. *Eos* **74**, 76.

Masters, G., Jordan, T. H., Silver, P. G. & Gilbert, F. 1982 Aspherical earth structure from fundamental spheroidal-mode data. *Nature* **298**, 609–613.

Montagner, J.-P. & Tanimoto, T. 1991 Global upper mantle tomography of seismic velocities and anisotropies. *J. Geophys. Res.* **96**, 20 337–20 351.

Nataf, H.-C., Nakanishi, I. & Anderson, D. L. 1986 Measurements of mantle wave velocities and inversion for lateral heterogeneities and anisotropy. 3. Inversion. *J. Geophys. Res.* **91**, 7261–7307.

Park III, J. F. L. & Lindberg, C. R. 1987 Frequency dependent polarization analysis of high-frequency seismograms. *J. Geophys. Res.* **92**, 12 664–12 674.

Parker, R. L. 1994 *Geophysical inverse theory.* Princeton University Press.

Pulver, S. & Masters, G. 1990 $PcP-P$ travel times and the ratio of S to P velocity variations in the lower mantle. *Eos* **71**, 1464.

Ricard, Y., Richards, M., Lithgow-Bertollini, C. & LeStunff, Y. 1993 A geodynamic model of mantle density heterogeneity. *J. Geophys. Res.* **98**, 21 895–21 909.

Ritzwoller, M., Masters, G. & Gilbert, F. 1986 Observations of anomalous splitting and their interpretation in terms of aspherical structure. *J. Geophys. Res.* **91**, 10 203–10 228.

Ritzwoller, M., Masters, G. & Gilbert, F. 1988 Constraining aspherical structure with low frequency interaction coefficients: application to uncoupled multiplets. *J. Geophys. Res.* **93**, 6369–6396.

Scott, J. S., Masters, T. G. & Vernon, F. L. 1994 3-D velocity structure of the San Jacinto fault zone near Anza, California. I. P waves. *Geophys. Journ. International* **119**, 611–626.

Shaw, P. R. & Orcutt, J. A. 1985 Waveform inversion of seismic refraction data and applications to young Pacific crust. *Geophys. Jl R. Astr. Soc.* **82**, 375–414.

Shearer, P. M. 1990 Seismic imaging of upper-mantle structure with new evidence for a 520 km discontinuity. *Nature* **344**, 121–126.

Shearer, P. M. 1991*a* Imaging global body wave phases by stacking long-period seismograms. *J. Geophys. Res.* **96**, 20 353–20 364.

Shearer, P. M. 1991*b* Constraints on upper mantle discontinuities from observations of long-period reflected and converted phases. *J. Geophys. Res.* **96**, 18 147–18 182.

Shearer, P. M. & Masters, G. 1992 Global mapping of topography on the 660 km discontinuity. *Nature* **355**, 791–796.

Smith, M. F. 1989 Imaging the Earth's aspherical structure with free oscillation frequency and attenuation measurements. Ph.D. thesis, University of California at San Diego, La Jolla, CA.

Smith, M. F. & Masters, G. 1989 Aspherical structure constraints from free oscillation frequency and attenuation measurements. *J. Geophys. Res.* **94**, 1953–1976.

Soller, D. R., Ray, R. D. & Brown, R. D. 1982 A new global crustal thickness model. *Tectonics* **1**, 125–149.

Su, W.-J. & Dziewonski, A. M. 1991 Predominance of long-wavelength heterogeneity in the mantle. *Nature* **352**, 121–126.

Su, W.-J., Woodward, R. L. & Dziewonski, A. M. 1994 Degree 12 model of shear velocity heterogeneity in the mantle. *J. Geophys. Res.* **99**, 6945–6980.

Tackley, P. J., Stevenson, D. J., Glatzmaier, G. A. & Schubert, G. 1993 Effects of an endothermic phase transition at 670 km depth on a spherical model of convection in the Earth's mantle. *Nature* **361**, 699–704.

Tackley, P. J., Stevenson, D. J., Glatzmaier, G. A. & Schubert, G. 1994 Effects of multiple phase transitions in a three dimensional spherical model of convection in Earth's mantle. *J. Geophys. Res.* **99**, 15 877–15 901.

Tanimoto, T. 1988 The 3-D shear wave structure in the mantle by overtone waveform inversion. II. Inversion of X-waves, R-waves and G-waves. *Geophys. Jl* **93**, 321–333.

Tanimoto, T. 1990 Long-wavelength S-velocity structure throughout the mantle. *Geophys. Jl Int.* **100**, 327–336.

Thomson, D. J. 1982 Spectrum estimation and harmonic analysis. *IEEE Proc.* **70**, 1055–1096.

Woodhouse, J. H. & Dahlen, F. A. 1978 The effect of a general aspherical perturbation on the free oscillations of the earth. *Geophys. Jl R. Astr. Soc.* **53**, 335–354.

Woodhouse, J. H. & Dziewonski, A. M. 1984 Mapping of the upper mantle: three-dimensional modeling of earth structure by inversion of seismic waveforms. *J. Geophys. Res.* **89**, 5953–5986.

Woodhouse, J. H. & Wong, Y. K. 1986 Amplitude, phase and path anomalies of mantle waves. *Geophys. Jl R. Astr. Soc.* **87**, 753–773.

Woodward, R. L. & Masters, G. 1991*a* Lower mantle structure from $ScS-S$ differential travel times. *Nature* **352**, 231–233.

Woodward, R. L. & Masters, G. 1991*b* Global upper mantle structure from long-period differential travel-times. *J. Geophys. Res.* **96**, 6351–6377.

Woodward, R. L. & Masters, G. 1992 Upper mantle structure from long-period differential travel times and free-oscillation data. *Geophys. J. International* **109**, 275–293.

Woodward, R. L., Forte, A. M., Su, W. & Dziewonski, A. M. 1993 *Constraints on the large-scale structure of the mantle* (Geophysical Monograph 74), IUGG, vol. 14 (ed. Takahashi *et al.*), pp. 89–109. Washington, DC: AGU.

Discussion

J. H. Davies (*Department of Earth Sciences, University of Liverpool, UK*). I have three comments regarding Dr Masters's statement that his tomographic inversion demonstrates a long wavelength nature for mantle seismic heterogeneity. First, since the data that he uses is of a long period it is not sensitive to short scale length mantle structure. Second, regional tomographic studies have shown us that the structure of the transition region of the mantle, for example, is dominated by short wavelength structure of subducting slabs. Third, his parametrization does not allow short scale length structure. Is it possible that either his seismic results are aliased or that the spectrum of seismic structure has a second significant peak at a much higher harmonic degree than present in his parametrization?

G. Masters. Dr Davies is correct that our long-period data are not sensitive to short wavelength structure. However, Fresnel zone arguments give an averaging scale of about 1000 km for our body-wave data implying sensitivity to structure up to about harmonic degree 40. The surface wave data at 80 s period have substantially shorter wavelengths and so can, in principle, sense even higher degree structure. It is therefore interesting that the spectral content of these data-sets is largely dominated by harmonic degrees less than 6. The data coverage is sufficiently good to preclude significant aliasing of short-wavelength structure but it is possible that the spectrum of seismic structure increases in amplitude at harmonic degrees greater than about 40 corresponding to wavelengths which are averaged out by our data.

My personal feeling is that the spectrum of seismic structure is qualitatively like the spectrum of topography of the Earth. We are all aware of large local variations in topography yet the amplitude spectrum of topography decreases monotonically as wavelength decreases and is dominated by the longest wavelengths. I suspect that the spectrum of seismic structure behaves in a similar manner. Of course there are regions of high-amplitude short-wavelength structure which we should be trying to incorporate into the global models, but such regions are not representative of the globe as a whole.

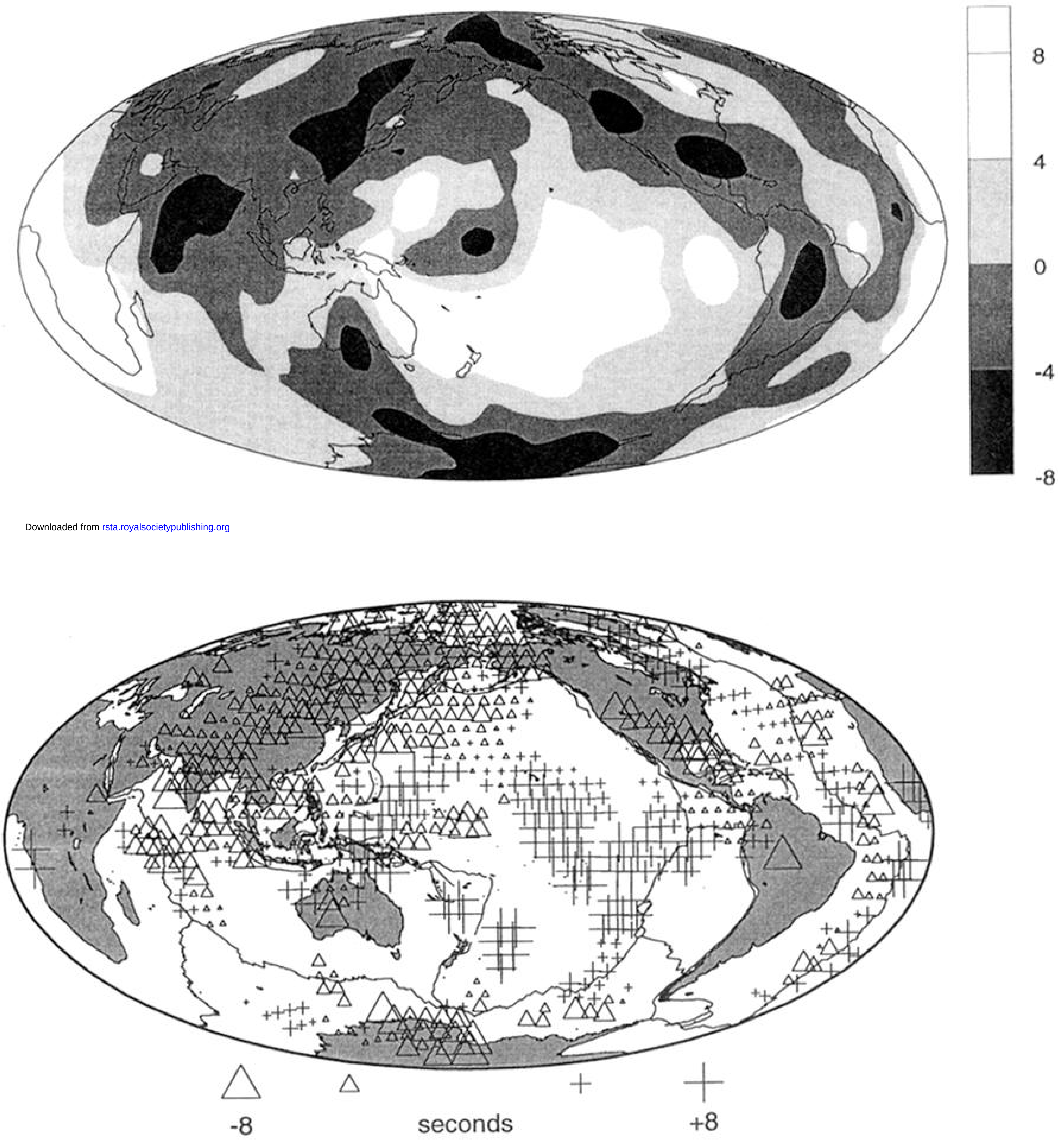

igure 3. Lower panel: long-period S residuals plotted at the turning point of S for rays which ottom in the lowermost 300 km of the mantle. The raw data have been lightly smoothed by pplying a running-mean smoothing filter which is a spherical cap of radius 5°. Note the ring of egative residuals (fast velocity) around the Pacific. The upper panel shows a map of the data onstructed using spherical splines. The contour levels are in seconds.

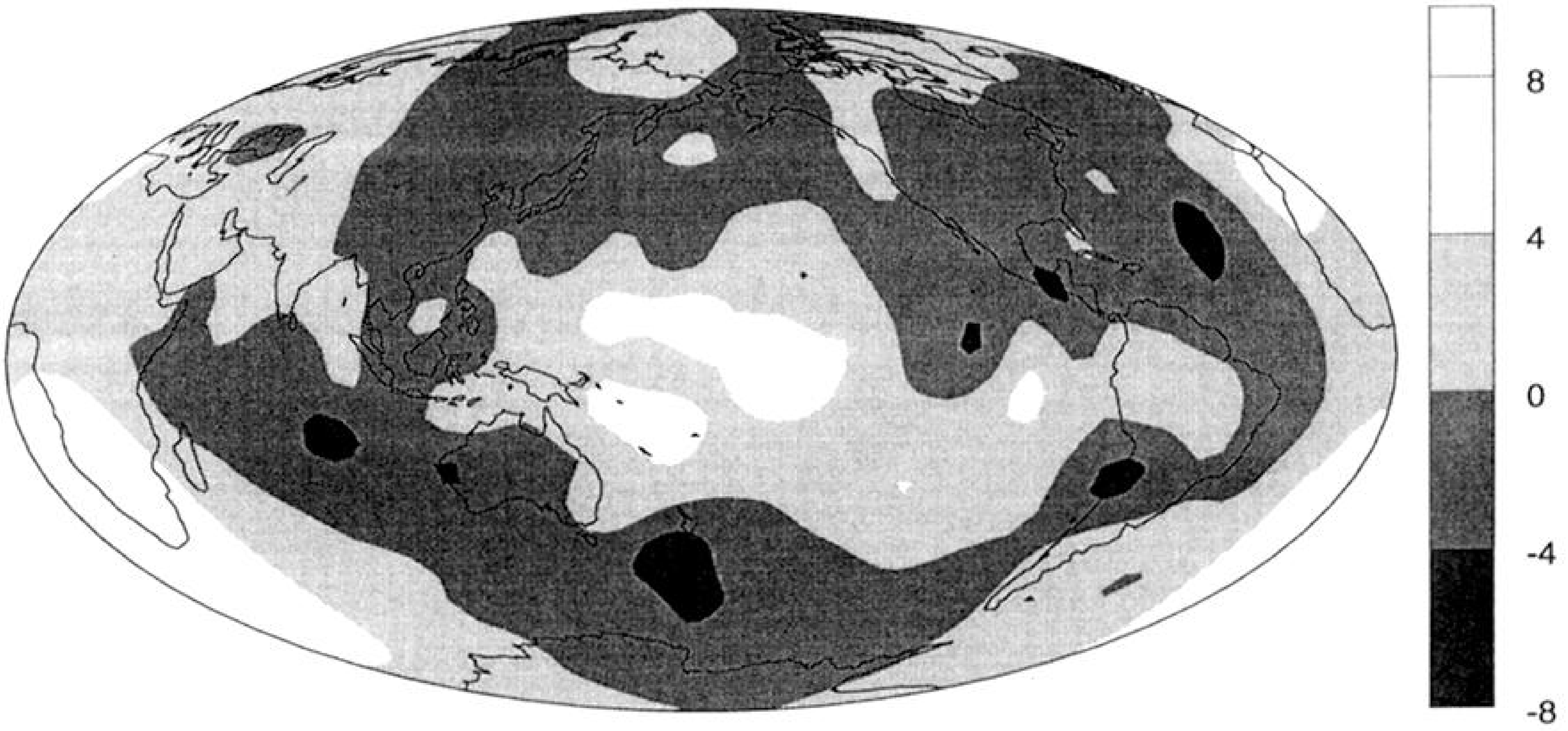

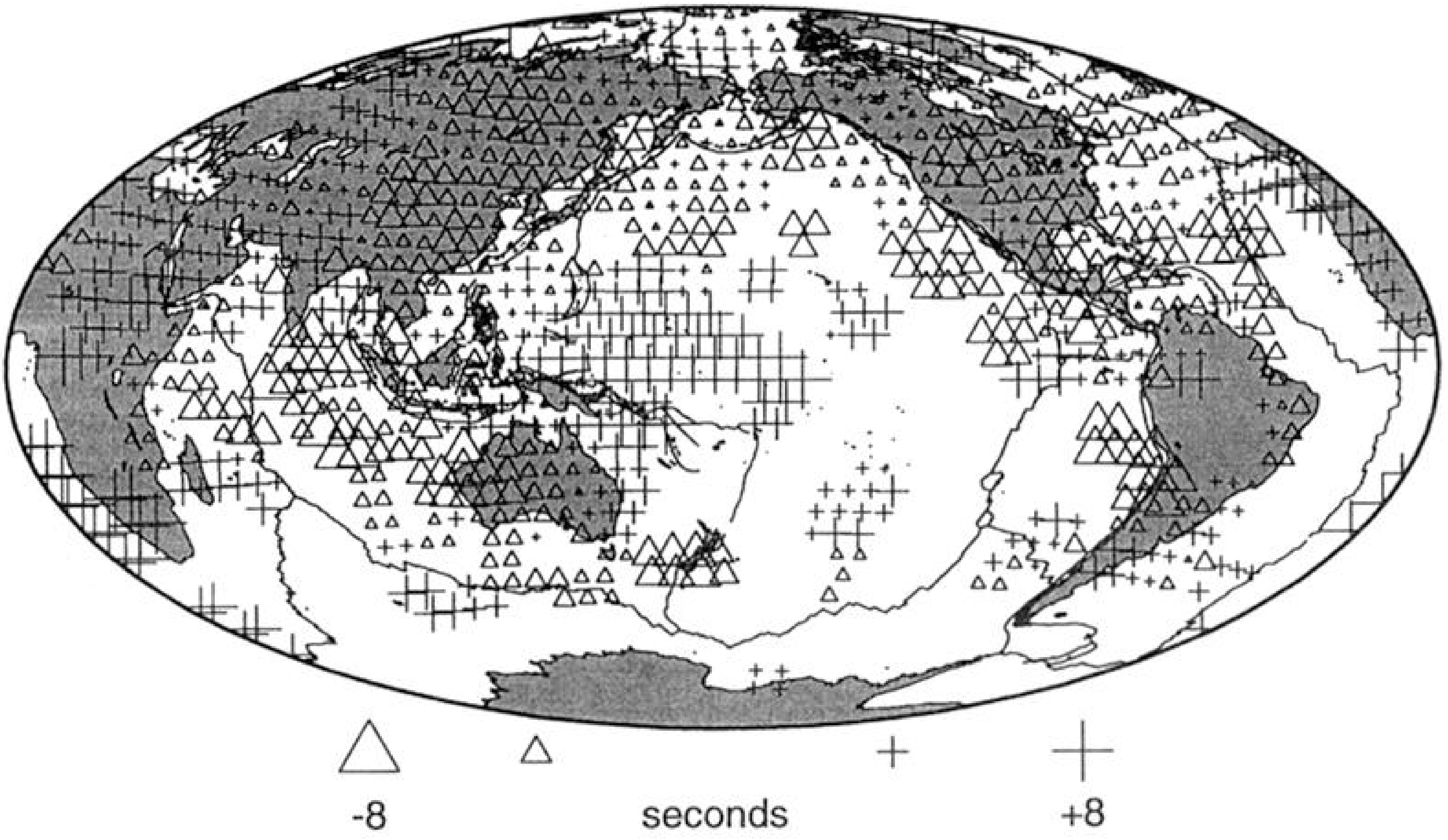

igure 4. Long-period $ScS - S$ residuals plotted at the bounce point of ScS on the core–mantle oundary (see figure 3 for details). Again, note the ring of negative residuals (fast velocity) round the Pacific.

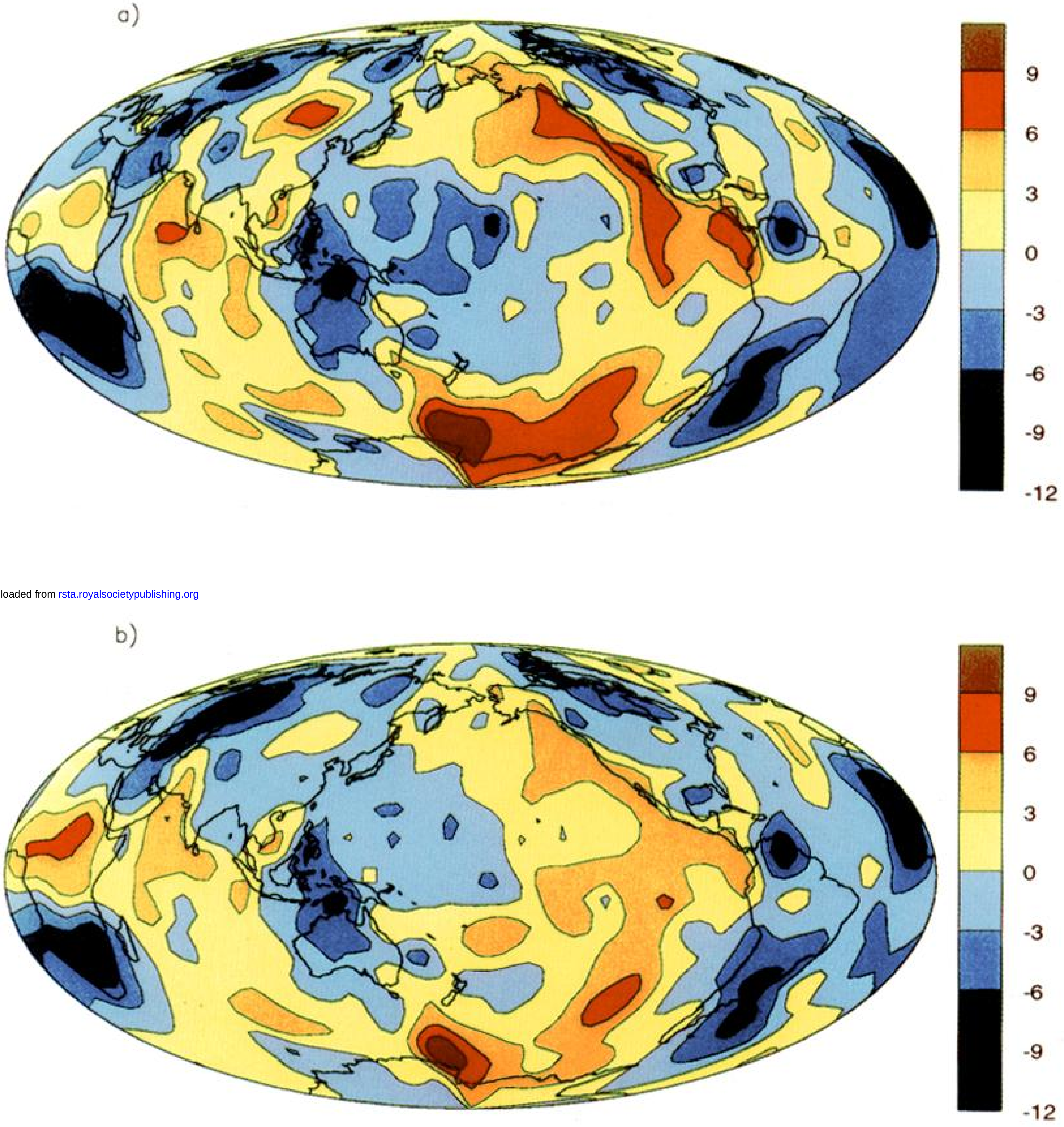

igure 5. Smoothed $SS - S$ residuals relative to PREM, constructed by fitting spherical splines o $SS - S$ residuals placed at their surface bounce points. Contour levels are in seconds. (*a*) is orrected for ellipticity and topography, and reflects both vertically averaged velocity structure n the upper mantle (from the SS leg) and low spherical harmonic degree structure in the lower nantle (from the S leg). (*b*) is constructed from the same data but is corrected for the traversal of he S leg through the lower mantle structure of model SH8/U4L8. (*b*) should represent vertically ntegrated upper mantle velocity structure, and fits a cooling halfspace velocity model of the ceanic crust better than (*a*).

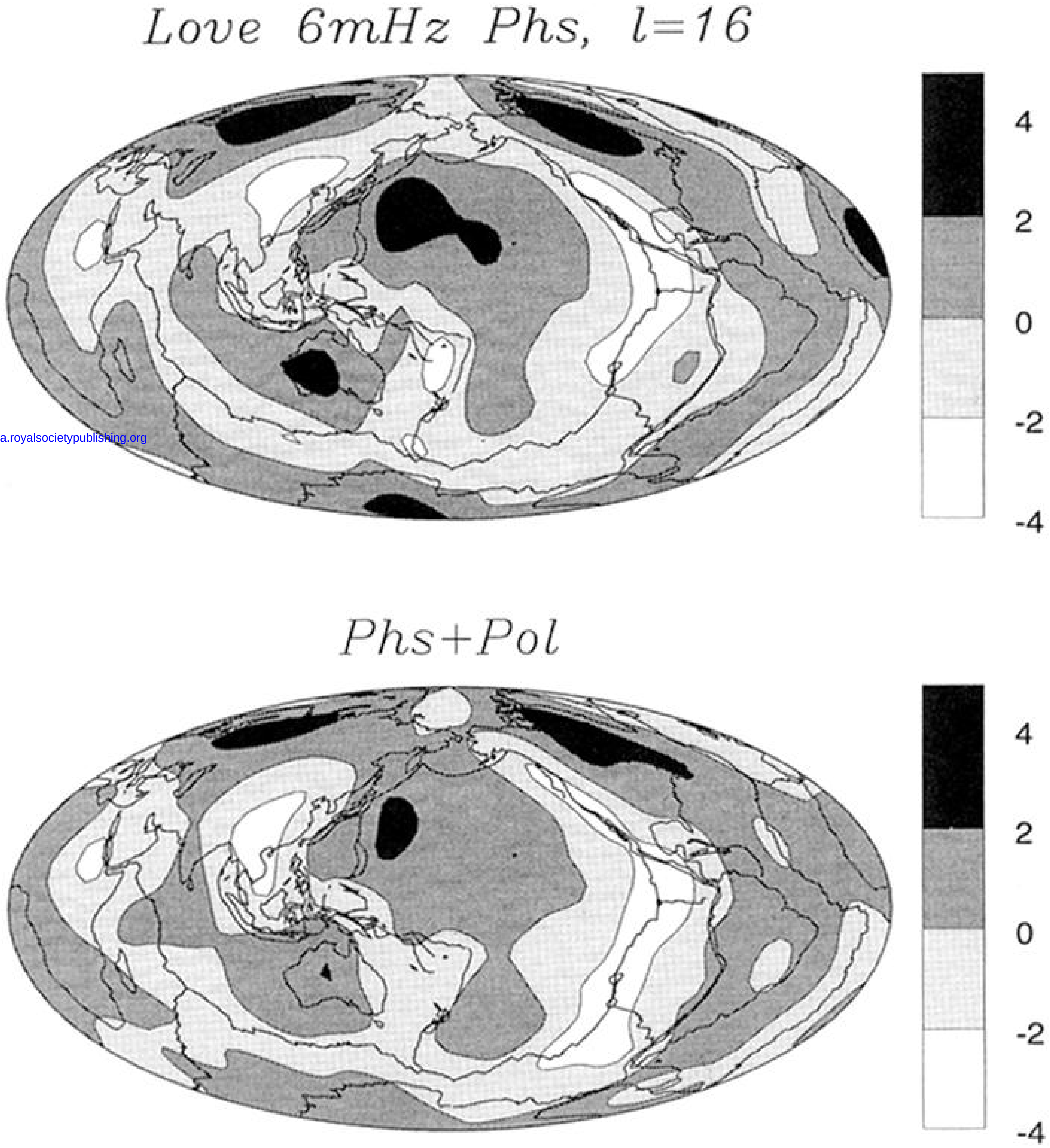

igure 6. Comparison of the phase velocity maps obtained for Love waves at 6 mHz. For the pper map, only phase data were used for the inversion, while phase and polarization data were sed to obtain the lower map. The maps are expanded in spherical harmonics up to degree $\ell = 16$ nd show phase velocity perturbation in %. The phase data do not require structure above $\ell = 12$ ut the fit of the polarization data can be dramatically improved by low amplitude structure etween $\ell = 12$ and 16.

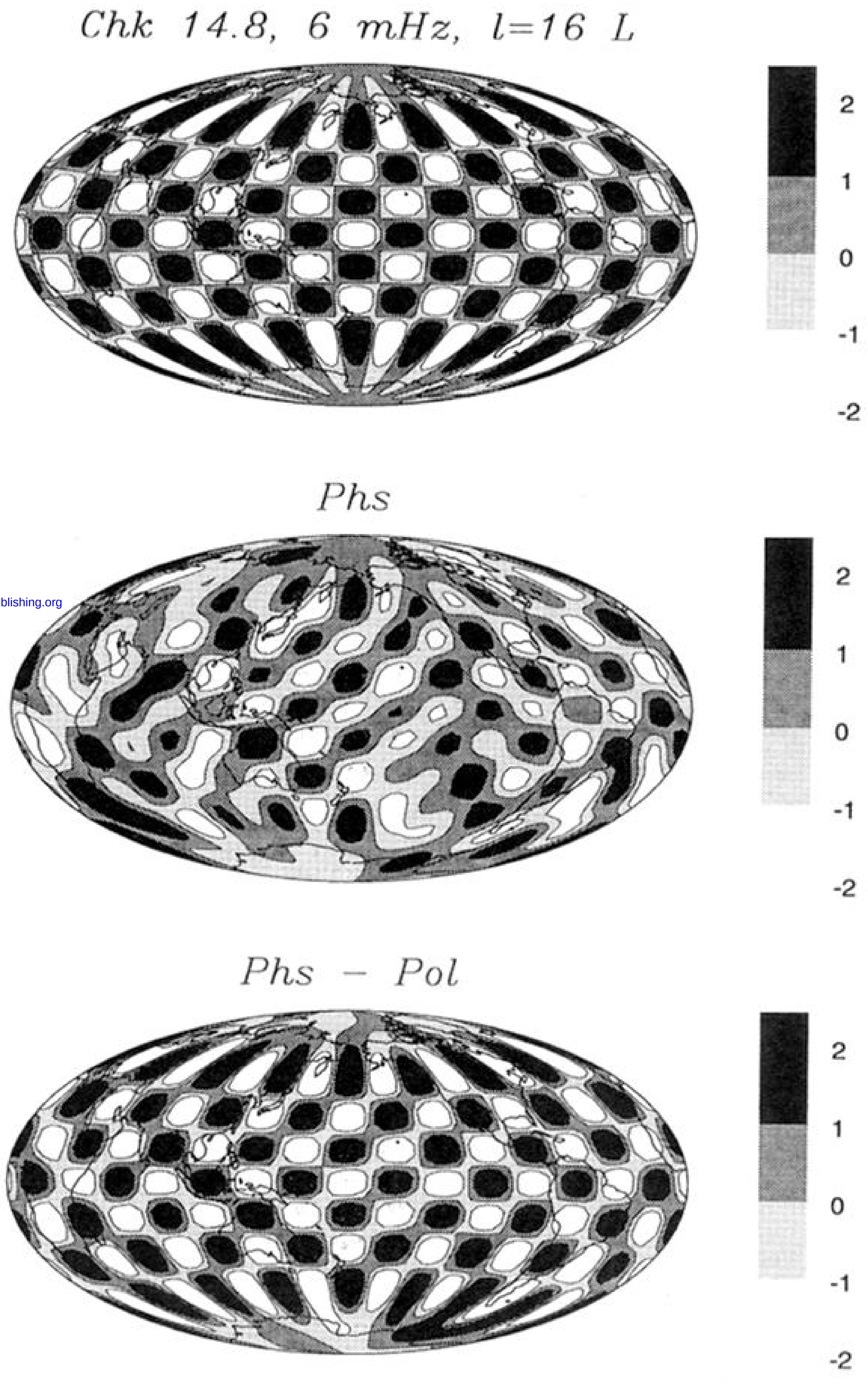

Figure 7. Resolution test using a Y_{14}^{8} checkerboard pattern (top panel). This test assumes that nonlinear effects are unimportant and inverts a synthetic data-set using the same operator that was used to invert the real data. The middle panel shows the recovery of the pattern when only phase data are included. The lower panel shows the recovery when phase and polarization data are used simultaneously in the inversion.

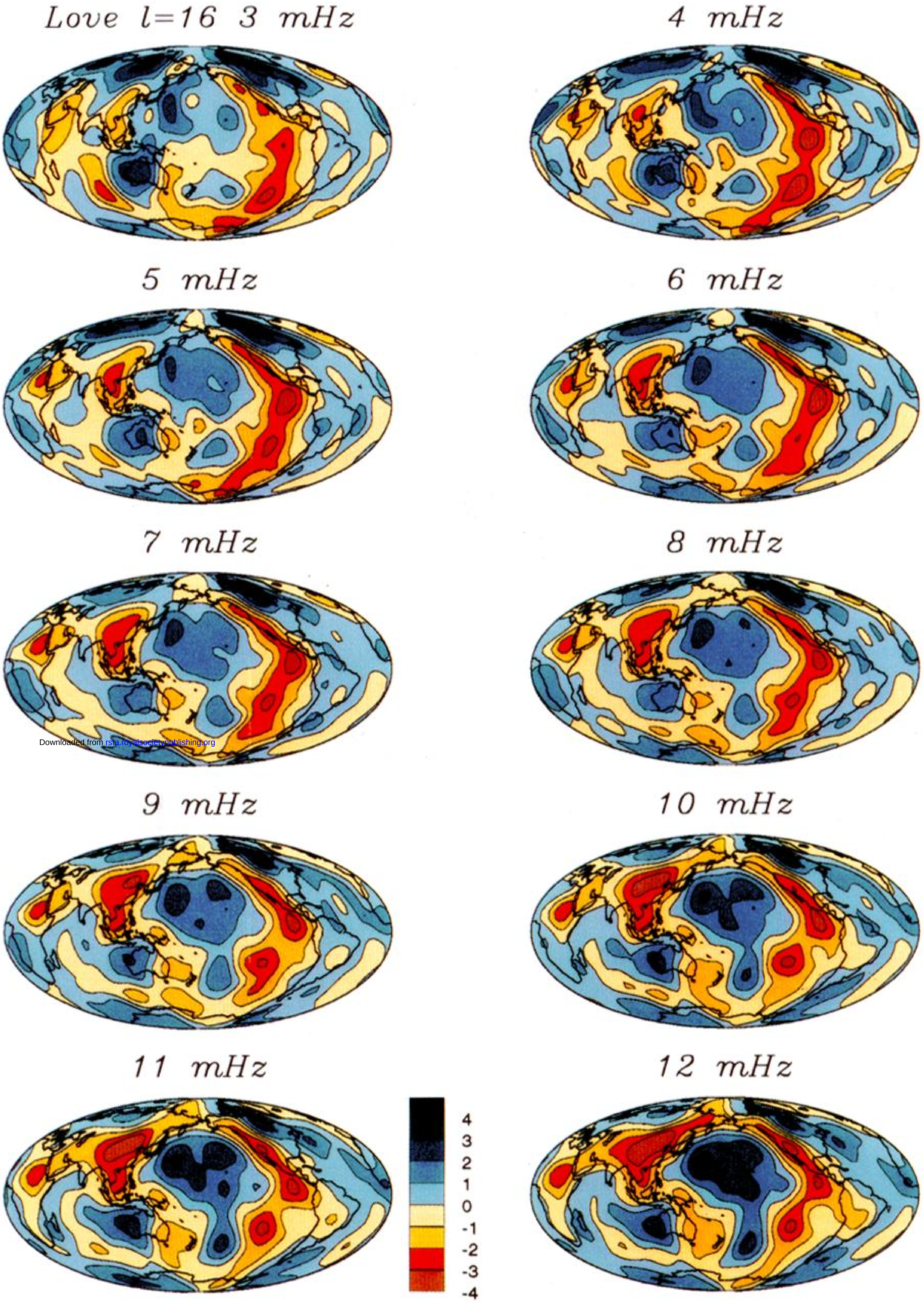

igure 8. The ten Love wave phase velocity maps obtained from a smoothed inversion of phase nd polarization data. The maps are expanded in spherical harmonics up to degree $\ell = 16$ and how phase velocity perturbation in %. The errors vary geographically and with frequency but o not exceed 0.3%.

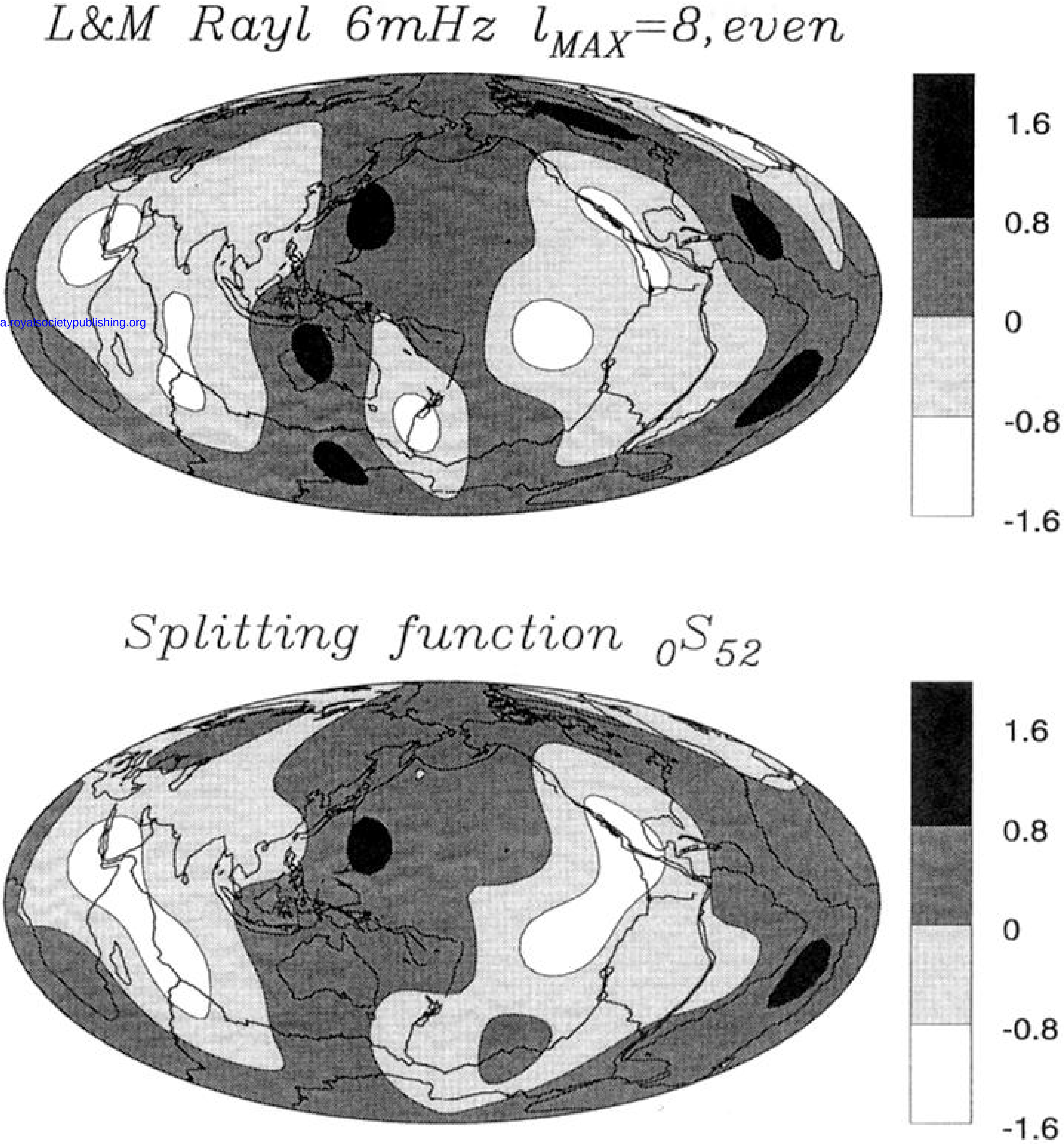

L&M Rayl 6mHz l_{MAX}=8, even

Splitting function ${}_0S_{52}$

igure 9. Comparison of the phase velocity map for Rayleigh waves at 6 mHz and the splitting unction of spheroidal fundamental mode ${}_0S_{52}$. Since the splitting function is expanded only up o $\ell = 8$, the phase velocity map was truncated at $\ell = 8$ and only even harmonic degrees are hown.

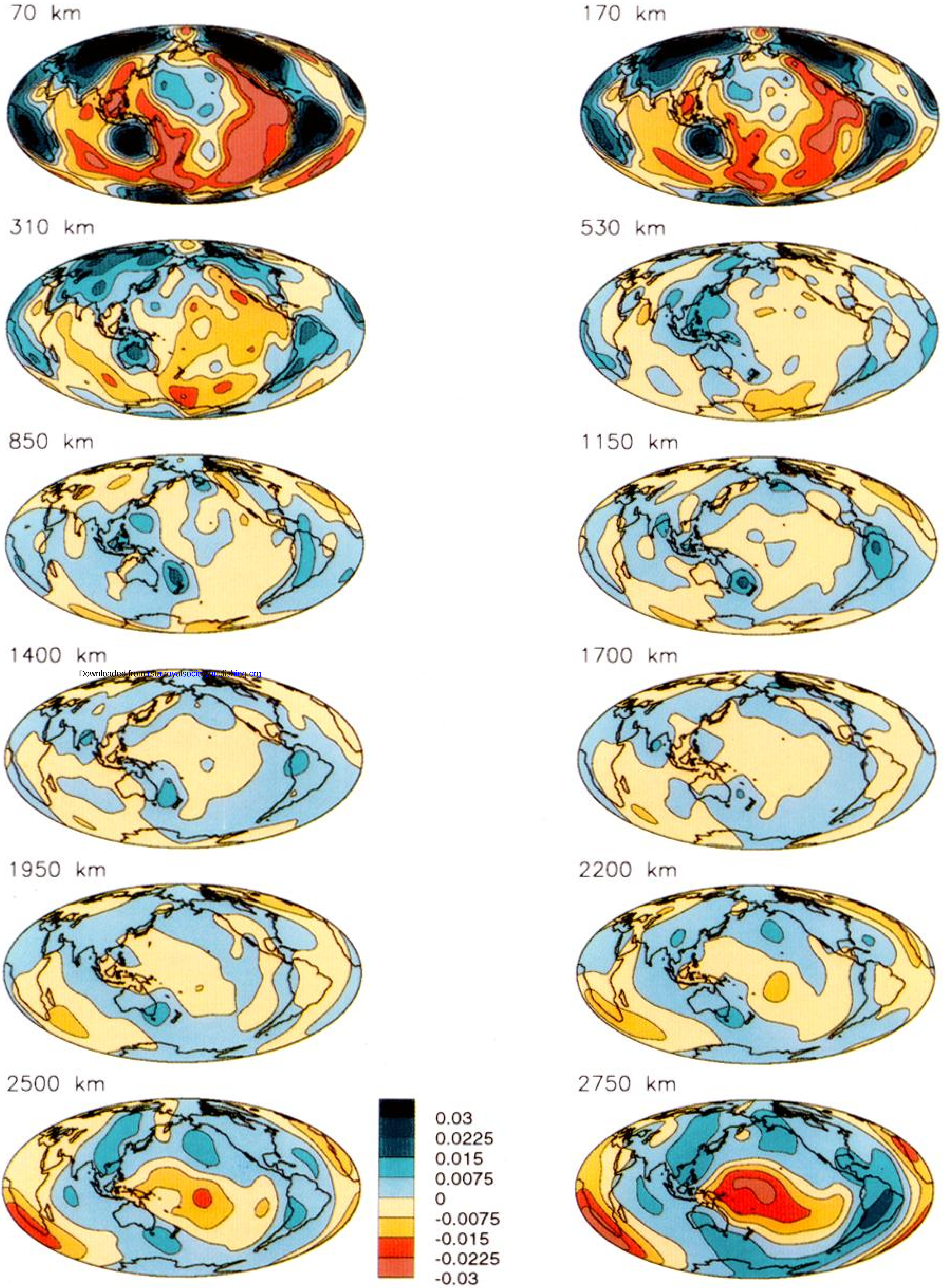

igure 13. Twelve depth slices of model S16B30. Contoured values are shear velocity perturbation relative to the global model average at a given depth.

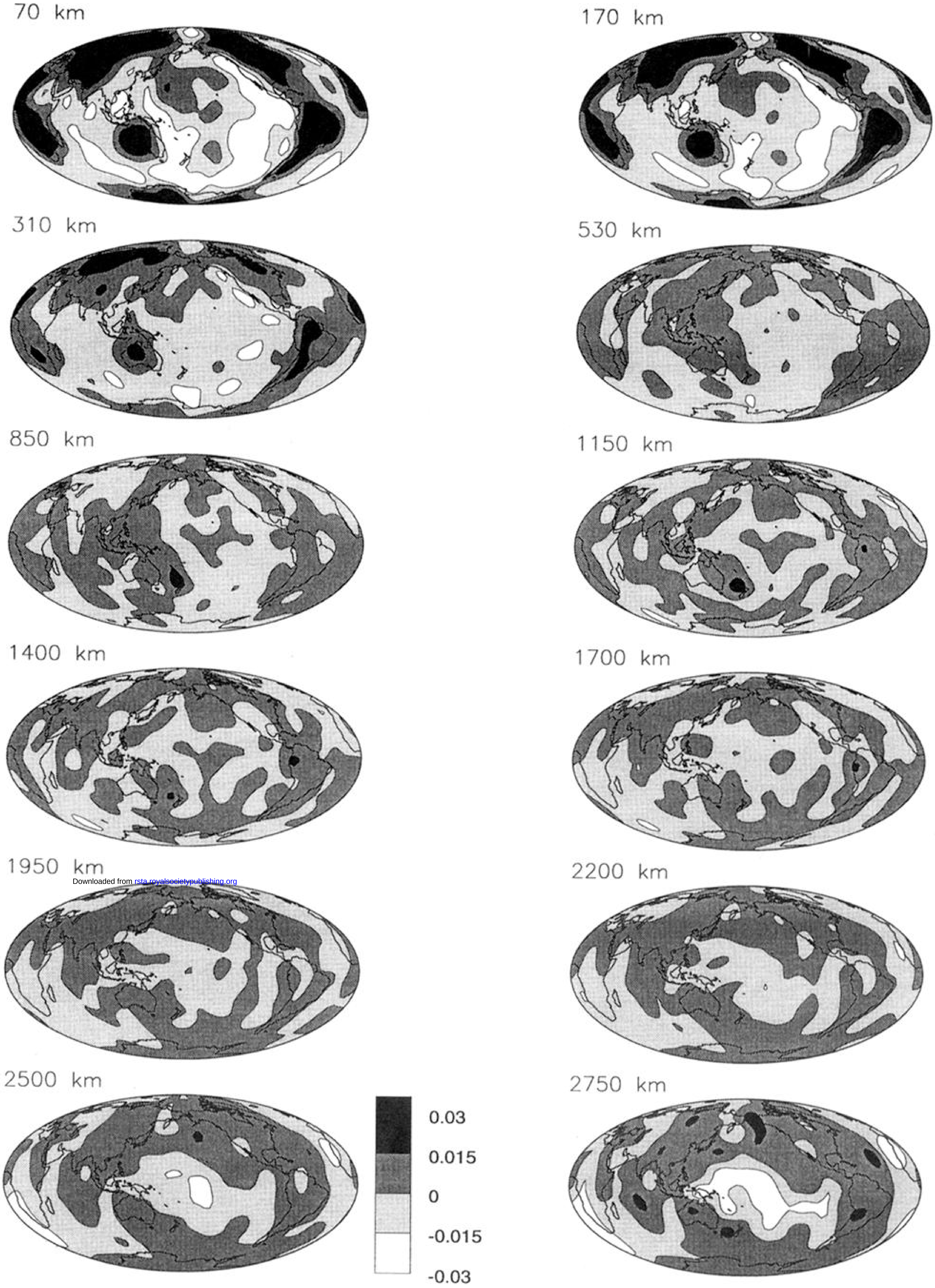

Figure 14. Model S16B30.2, plotted as in figure 13. While radially smoother than S16B30 (figure 13), this model is laterally rougher, as is especially evident in the comparison of the lower mantle slices of figures 13 and 14. Even though the total data misfit expresses no preference for model S16B30 against S16B30.2, it is argued that S16B30 is a better compromise amongst the misfits shown in figure 12, and that S16B30.2 posseses spurious structure when compared to data sets such as $ScS - S$.

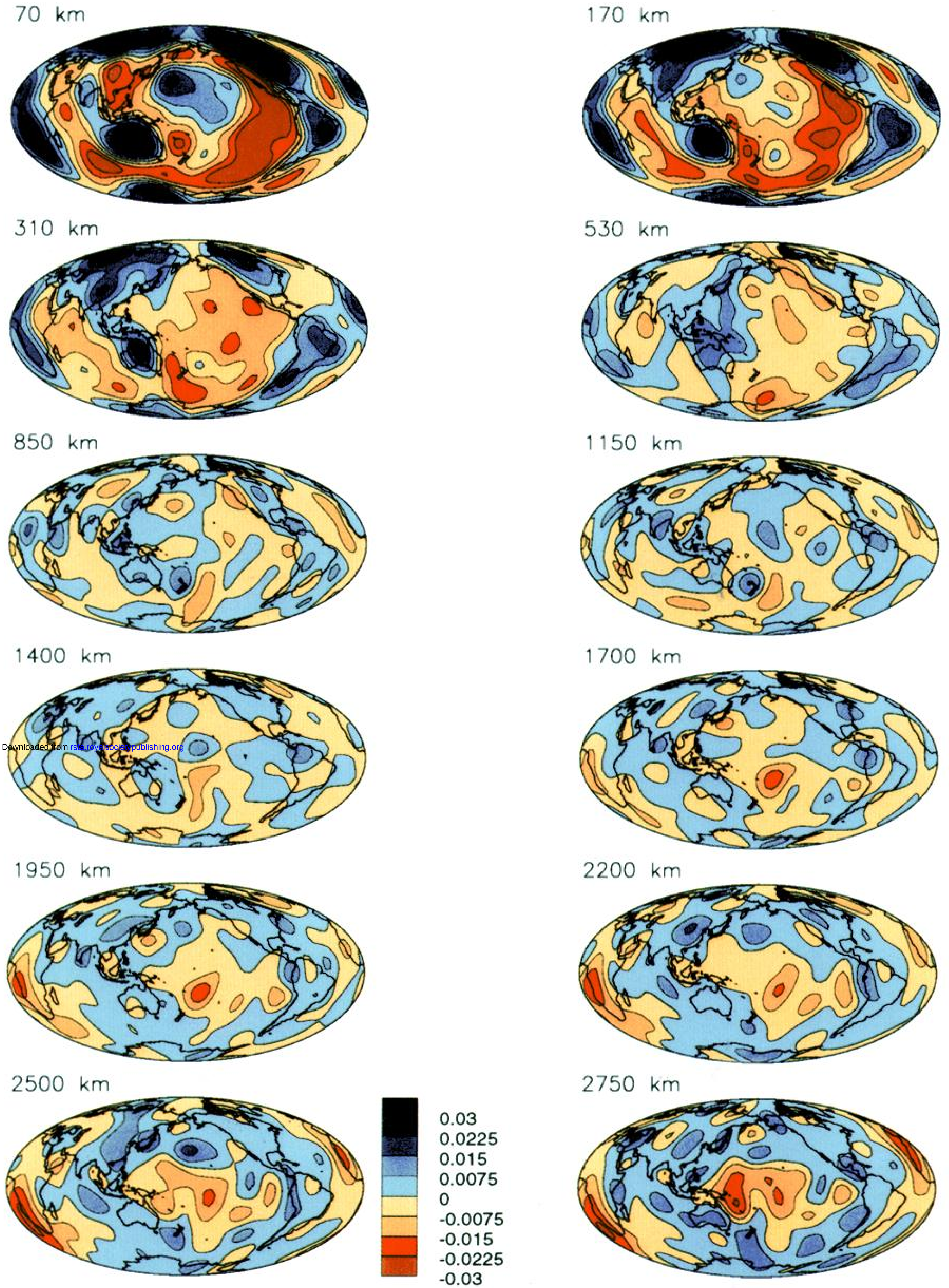

igure 15. Model SH12WM13 plotted as in figure 13. All the models presented here have a elatively small fraction of data in common (part of the $SS-S$ and $ScS-S$ data-sets), but were btained by different methods and employ different radial basis functions. The main differences etween S16B30 (figure 13) and SH12WM13 are in the patterns of mid-mantle structure and in he size of anomalies in the lowermost mantle.

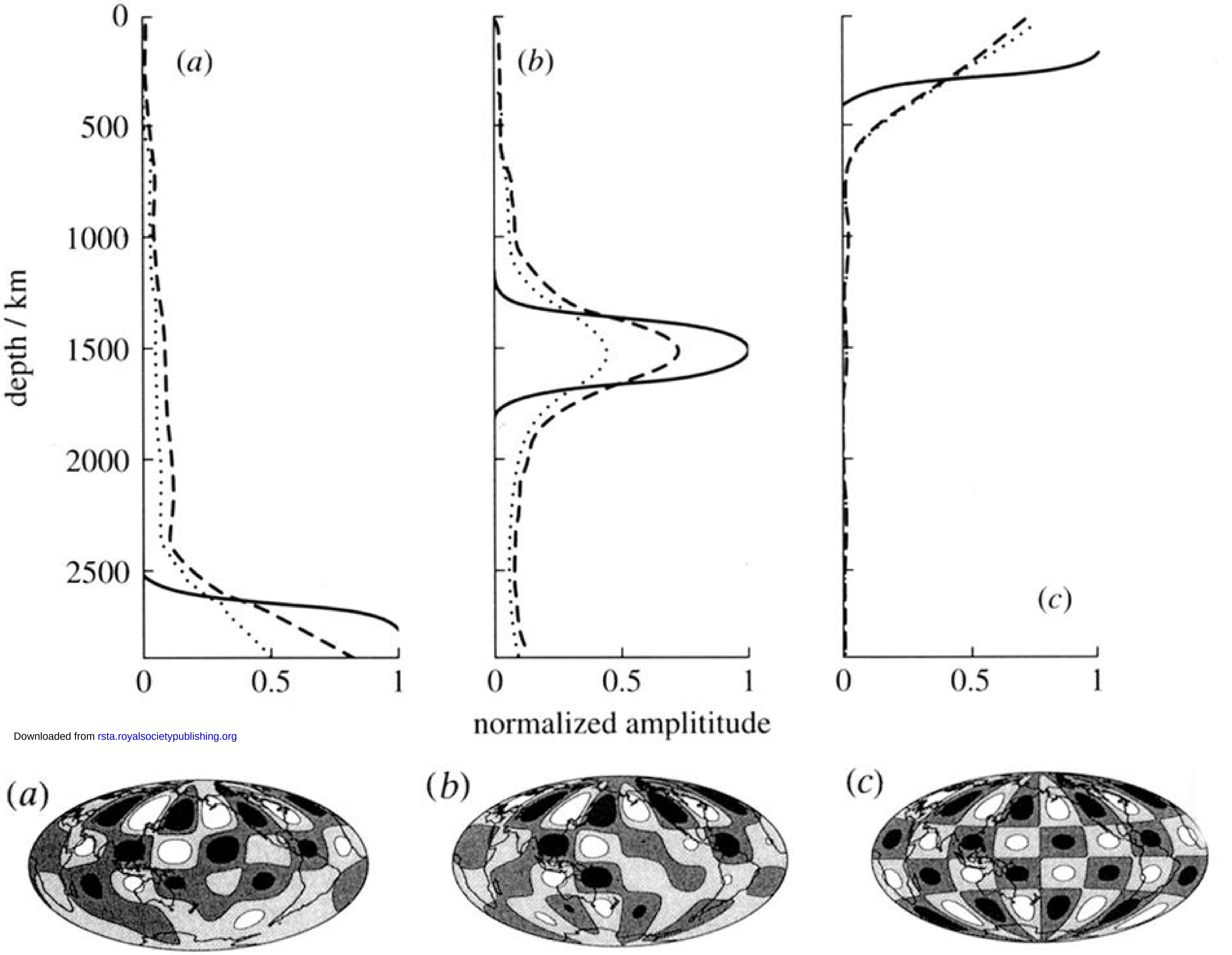

igure 17. Attempts to recover checkerboard patterns at three levels in the mantle. The input attern is the linear combination of three natural B-splines in radius and is a Y_7^4 spherical armonic laterally. The solid curve in the upper plots is the amplitude against depth of the nput pattern, normalized to have a peak value of 1. The dashed line is the peak recovered alue at each depth as a fraction of the input pattern peak at that depth. The dotted line is he fraction of the RMS amplitude recovered. The lower plots show the recovered pattern at the epth of the peak recovered RMS. Although not shown, the input pattern is essentially identical o the recovered pattern in (*c*). (*a*) An attempt to recover a checkerboard pattern situated at he bottom of the mantle (the bottom three B-splines). Although some of the input pattern is meared into low amplitudes across the lower mantle, the radial resolution is taken to be the ncrease in radial extent of the main peak of the recovered pattern which is roughly 200 km. The ifference in the fraction of recovered RMS and peak amplitudes is due to the geographic variation f the resolution. (*b*) An attempt to recover a checkerboard pattern situated in the mid-mantle. s in (*a*), the input pattern is the linear combination of three B-splines in radius. The edges of he input peak are smeared 200–300 km radially. (*c*) Attempt to recover a checkerboard pattern ituated in the upper mantle. The model construction algorithm tends to smear the anomaly bout 200 km radially although the shape is very well-recovered.

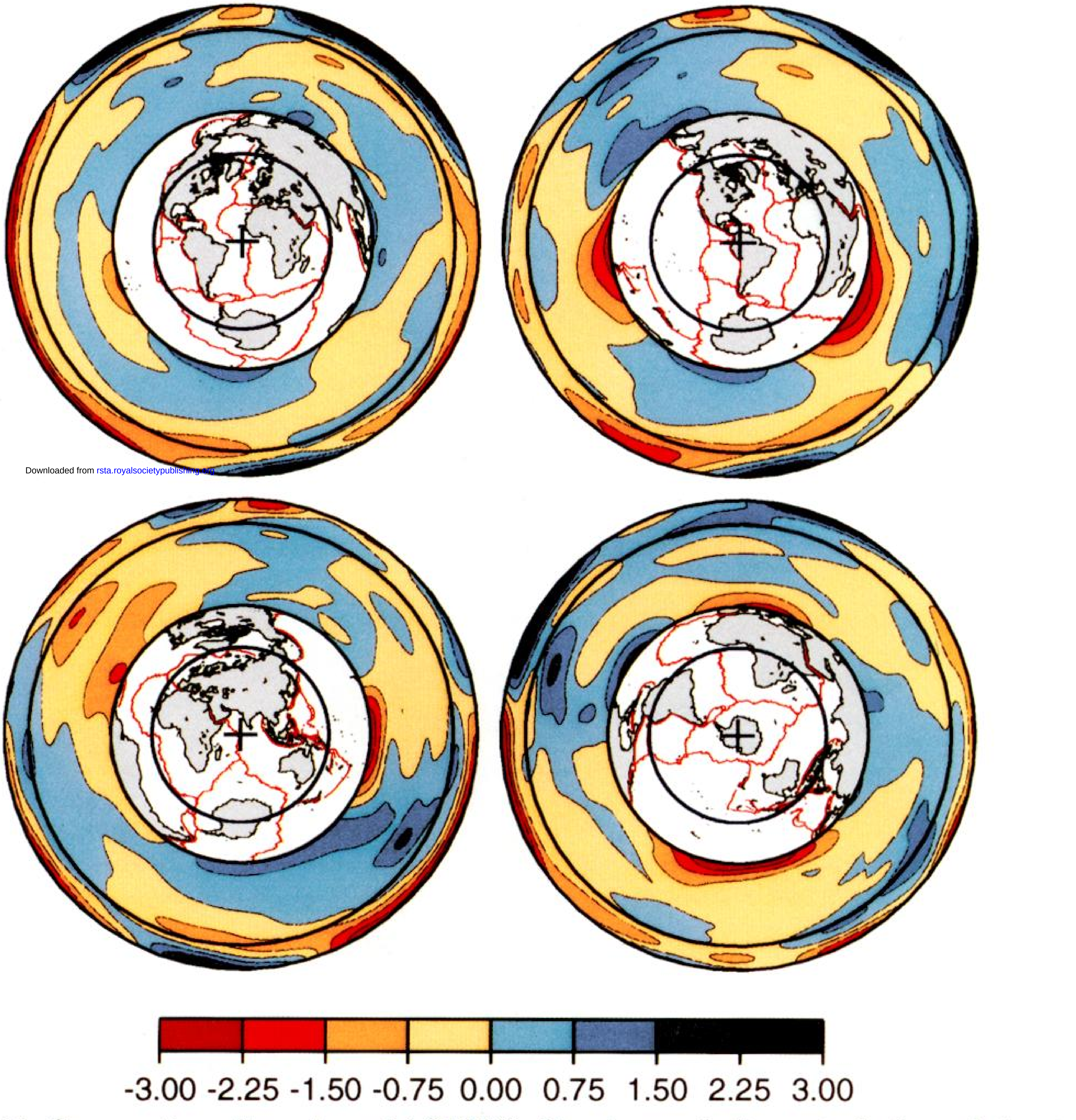

igure 18. Cross-sections through model S16B30. The shear velocity perturbation relative to he model average at depth is contoured. The slices intersect the surface along the great circles lotted on azimuthal equidistant projections in the centres of the cross sections.